

MAP, MAC, and Vortex-rings Configurations in the Weinberg-Salam Model*

Rosy Teh[†], Ban-Loong Ng and Khai-Ming Wong

School of Physics, Universiti Sains Malaysia
11800 USM Penang, Malaysia

May 21, 2014

Abstract

We report on the presence of new axially symmetric monopoles, anti-monopoles and vortex-rings solutions of the $SU(2) \times U(1)$ Weinberg-Salam model of electromagnetic and weak interactions. When the θ -winding number $n = 1$, and 2, the configurations are monopole-antimonopole pair (MAP) and monopole-antimonopole chain (MAC) with poles of alternating sign magnetic charge arranged along the z -axis. Vortex-rings start to appear from the MAP and MAC configurations when the winding number $n = 3$. The MAP configurations possess zero net magnetic charge whereas the MAC configurations possess net magnetic charge of $4\pi n/e$. In the MAP configurations, the monopole-antimonopole pair is bounded by the Z^0 field flux string and there is an electromagnetic current loop encircling it. The monopole and antimonopole possess magnetic charges $\pm \frac{2\pi n}{e}$ respectively. In the MAC configurations there is no string connecting the monopole and the adjacent antimonopole and the monopole and antimonopole possess magnetic charges $\pm \frac{4\pi n}{e}$ respectively. The MAC configurations possess infinite total energy and zero magnetic dipole moment whereas the MAP configurations which are actually sphalerons possess finite total energy and magnetic dipole moment. The configurations were investigated for varying value of Higgs field mass $0 \leq \mu^2 \leq 40$ at Weinberg angle $\theta_W = \frac{\pi}{4}$.

1 Introduction

Magnetic monopole was first introduced into the Maxwell theory by P.A.M. Dirac [1]. The presence of the magnetic monopole with pole strength g leads to the

*To be submitted for publication

[†]E-mail: rosyteht@usm.my

requirement that all electric charges have to be quantized in integral multiples of a unit electric charge e given by the formula $\frac{qe}{\hbar c} = \frac{1}{2}n$. The fact that electric charges are quantized and that there are no other explanation for this quantization makes magnet monopole a very important particle that has yet to be discovered. The magnetic field of the Dirac monopole carries a string singularity.

In 1969, a non-Abelian magnetic monopole with only a point singularity was found as a solution to the pure SU(2) Yang-Mills theory by Wu and Yang [2]. However both the Dirac and Wu-Yang monopole possess infinite energy due to the presence of a point singularity in the solution. It was in 1974 that a finite energy magnetic monopole was found by 't Hooft and Polyakov [3] independently in the SU(2) Georgi-Glashow model. The mass of the 't Hooft-Polyakov monopole was calculated to be of order $137 M_W$, where M_W is the mass of the intermediate vector boson. In the Georgi-Glashow model, $M_W < 53$ GeV, however the mass is given by $M_W = 80.385 \pm 0.015$ GeV in the Particle Physics Booklet [4]. Hence the mass of the magnetic monopole in the Georgi-Glashow model is of the order of 11 TeV.

A few years later in 1977, Y. Nambu found string-like configurations in the SU(2) \times U(1) Weinberg-Salam model [5]. These configurations are a monopole-antimonopole pair bound by a flux string of the \mathcal{Z}^0 field. The total energy of this MAP configuration is finite and the mass of the monopole and antimonopole together with the string is estimated to be in the TeV range. At asymptotically large distances, the real electromagnetic field is a linear combination of U(1) and SU(2) gauge fields created by the MAP. The flux through the string connecting the monopole and antimonopole is U(1) whereas the flux of the monopole and antimonopole is SU(2). Although the arguments and calculations presented are not rigorous, but the existence of massive string-like MAP configurations of the Weinberg-Salam theory had been accurately predicted by Nambu. Our numerical results for the 1-MAP and 2-MAP configurations given in Section 4.3 here confirmed Nambu's finding years ago [5].

After Nambu's work [5], there is a large amount of work done on the classical solutions of the Weinberg-Salam theory [5] - [13], which is a hybrid of the Abelian Maxwell and the non-Abelian Georgi-Glashow theory. A well known solution of the Weinberg-Salam theory is the "sphaleron", first coined by Klinkhamer and Manton [7], which possesses baryon number $Q_B(\text{sphaleron}) = \frac{1}{2}$. A sphaleron is particle-like, static, localized in space and unstable. In this solution, Klinkhamer and Manton [7] noticed that there is an electric current in the U(1) field.

Numerous interesting work done on sphaleron include the work of Hindmarsh and James [8] and Radu and Volkov [9] which state that within the sphaleron there is a monopole-antimonopole pair and a loop of electromagnetic current. However in these works on sphaleron [6] - [9], there is no full solution to the equations of motion. The system is only solved locally near the region of the MAP poles and in the region of the Higgs vacuum.

In our numerical work we solved the equations of motion over all space and obtained full solutions to the Weinberg-Salam theory. Our 1-MAP and 2-MAP

configurations once again confirmed the findings of Ref. [6] - [9]. We found that the 1-MAP is a sphaleron with baryon number $Q_B = \frac{n}{2}$ and the 2-MAP configuration is a sphaleron and an anti-sphaleron with baryon number $Q_B = 0$. There is an electromagnetic current loop going round each magnetic dipole and the monopole and antimonopole in each pair are joined by a Z^0 field flux string. However in our MAP solutions, we note that the Weinberg angle θ_W is not arbitrary but can only take the value of $\theta_W = \frac{\pi}{4}$. When the ϕ -winding number $n = 1$, the monopoles and antimonopoles possess magnetic charges $\pm \frac{2\pi}{e}$ respectively which is half the magnetic charge of a Cho-Maison monopole.

Other work on sphalerons include the work of Ref. [10] and [11] which is a series of work using the same ansatz and definition. In these papers, no monopole-antimonopole pair or current loop is found in the sphaleron. The magnetic ansatz is used for the SU(2) gauge field which is the same ansatz as our work here but the solutions reported in Ref. [10] and [11] differ from our solutions. This is because the profile functions for the Higgs field differ from our profile functions of the Higgs field and their numerical results failed to reveal the inner structure of the sphaleron and anti-sphaleron. They also failed to obtain the MAC configurations with their numerical calculations.

In 1997, Cho and Maison [12] reported on the single monopole configuration in the Weinberg-Salam theory which is the same as the first solution in our MAC series of solutions. Similar to the Georgi-Glashow model, this configuration is spherically symmetrical. This electrically charged single monopole possesses magnetic charge $4\pi/e$. The apparent string singularity of this monopole along the negative z -axis of the U(1) gauge field is a pure gauge artifact that can be removed with a hypercharge U(1) gauge transformation. Hence unlike the MAP solution [5] - [9], this monopole does not possess a string. The total energy of this single monopole configuration is infinite due the point magnetic charge of the U(1) field. However by using various method discussed in Ref. [13], this electroweak monopole mass is estimated to be about 4 to 7 TeV which is within the range of the recent MoEDAL detector at LHC, CERN [14]. Hence there is a possibility that this Cho-Maison monopole can be detected by the experiment.

In this paper, we present numerical MAP, MAC and vortex-rings configurations that are axially symmetrical. Similar to the Georgi-Glashow theory, the only spherically symmetrical monopole solution is the single monopole with magnetic charge $4\pi/e$ that was found by Cho and Maison [12]. The other monopole configurations are at most axially symmetrical.

We solved the SU(2)×U(1) Weinberg-Salam equations of motion numerically over all space for presence of new axially symmetric electrically neutral monopole configurations. The solutions found are monopole-antimonopole pairs (MAP) and monopole-antimonopole chains (MAC) configurations when the θ -winding number $n = 1$ and 2. Vortex-ring configurations start to appear from the MAP and MAC configurations when the winding number $n = 3$.

The MAP configurations possess zero net magnetic charge and Weinberg angle $\theta_W = \frac{\pi}{4}$. The 1-MAP is a sphaleron with baryon number $Q_B = \frac{n}{2}$ and the 2-MAP

is a sphaleron anti-sphaleron pair with baryon number $Q_B = 0$. When $n = 1$ and 2, the monopole-antimonopole pair is bounded by the \mathcal{Z}^0 field flux string. When $n = 1$, the monopole and antimonopole possess magnetic charges $\pm \frac{2\pi}{e}$ respectively and hence they are half Cho-Maison monopole and antimonopole.

Similar to the results discussed by others [5] - [9], the MAP configurations or sphalerons found here possess finite total energy and magnetic dipole moment. Each monopole-antimonopole pair ($n = 1, 2$) and vortex-ring ($n = 3$) are surrounded by an electromagnetic current loop. The total energy is finite because there is no magnetic monopole presents in the U(1) field but just external electric current loops that provide the magnetic dipole moment of the U(1) field.

In the MAC configurations there is no string connecting the monopole and the adjacent antimonopole. When $n = 1$, the monopole and antimonopole possess magnetic charges $\pm \frac{4\pi}{e}$ respectively. Hence the monopole and antimonopole are whole Cho-Maison monopole and antimonopole. Since the MAC configurations possess odd number of poles, their net magnetic charge is $4\pi n/e$. The total energy of these MAC solutions is infinite due the point magnetic charge of the monopole in the U(1) field as discussed by Cho and Maison [12] for their one monopole solution. However the SU(2) part of the total energy is finite. This is expected as the energy of all the monopole solutions in the SU(2) Georgi-Glashow model is finite whereas the energy of a point charge in the Abelian U(1) theory blows up at the point. The MAC configurations do not possess magnetic dipole moment and unlike the MAP configurations, the Weinberg angle can take any value of $0 \leq \theta_W \leq \frac{\pi}{2}$.

In the next Section, we briefly present the Weinberg-Salam model and in Section 3 we obtained the reduced equations of motion by using the axially symmetrical magnetic ansatz. The MAC, MAP, and vortex-rings configurations are discussed and investigated in Section 4 for values of Higgs field mass $0 \leq \mu^2 \leq 40$ at Weinberg angle $\theta_W = \frac{\pi}{4}$. When $n = 1$ and 2, the MAC configurations presented are the one pole, three poles, and five poles solutions and the MAP configurations presented are the two poles and four poles solutions. When $n = 3$, vortex-rings configurations are found. We end with some comments in Section 5.

2 The Standard Weinberg-Salam Model

The Lagrangian in the standard Weinberg-Salam model is given by [12], [13]

$$\mathcal{L} = -(\mathcal{D}_\mu \phi)^\dagger (\mathcal{D}^\mu \phi) - \frac{\lambda}{2} (\phi^\dagger \phi - \zeta^2)^2 - \frac{1}{4} \mathbf{F}_{\mu\nu} \cdot \mathbf{F}^{\mu\nu} - \frac{1}{4} G_{\mu\nu} G^{\mu\nu}, \quad (1)$$

$$\mathcal{D}_\mu \phi = \left(D_\mu - \frac{ig'}{2} B_\mu \right) \phi, \quad D_\mu = \partial_\mu - \frac{ig}{2} \boldsymbol{\sigma} \cdot \mathbf{A}_\mu, \quad (2)$$

where \mathcal{D}_μ is the covariant derivative of the SU(2) \times U(1) group and D_μ is the covariant derivative of the SU(2) group only. The gauge coupling constant, potentials, and electromagnetic fields of the SU(2) group are given by g , $\mathbf{A}_\mu = A_\mu^a (\frac{\sigma^a}{2i})$, and $\mathbf{F}_{\mu\nu} = F_{\mu\nu}^a (\frac{\sigma^a}{2i})$ respectively, whereas the U(1) group's gauge coupling constant, potentials, and electromagnetic fields are given g' , B_μ , and $G_{\mu\nu}$ respectively. The σ^a

are Pauli matrices. The complex scalar Higgs doublet is ϕ , the Higgs field potentials' strength is λ and Higgs field mass is μ . The Higgs field vacuum expectation value is given by $\zeta = \frac{\mu}{\sqrt{\lambda}}$. The metric used is $-g_{00} = g_{11} = g_{22} = g_{33} = 1$.

The equations of motion that follow from Lagrangian (1) are

$$\mathcal{D}^\mu \mathcal{D}_\mu \phi = \lambda (\phi^\dagger \phi - \zeta^2) \phi, \quad (3)$$

$$D^\mu \mathbf{F}_{\mu\nu} = -\mathbf{j}_\nu = \frac{ig}{2} \{ \phi^\dagger \boldsymbol{\sigma} (\mathcal{D}_\nu \phi) - (\mathcal{D}_\nu \phi)^\dagger \boldsymbol{\sigma} \phi \}, \quad (4)$$

$$\partial^\mu G_{\mu\nu} = -k_\nu = \frac{ig'}{2} \{ \phi^\dagger (\mathcal{D}_\nu \phi) - (\mathcal{D}_\nu \phi)^\dagger \phi \}. \quad (5)$$

The Higgs field can also be written as

$$\begin{aligned} \phi &= |\Phi| \boldsymbol{\xi}, \quad \boldsymbol{\xi}^\dagger \boldsymbol{\xi} = 1, \\ \hat{\Phi}^a &= \boldsymbol{\xi}^\dagger \sigma^a \boldsymbol{\xi}, \quad \sigma^a = \begin{pmatrix} \delta_3^a & \delta_1^a - i\delta_2^a \\ \delta_1^a + i\delta_2^a & -\delta_3^a \end{pmatrix} \end{aligned} \quad (6)$$

where $|\Phi|$ is the Higgs modulus, $\boldsymbol{\xi}$ is a column 2-vector, and $\hat{\Phi}^a$ is the Higgs field unit vector. The energy density of Lagrangian (1) is given by

$$\begin{aligned} \mathcal{E} &= \frac{1}{4} F_{ij}^a F_{ij}^a + \frac{1}{2} F_{i0}^a F_{i0}^a + \frac{1}{4} G_{ij} G_{ij} + \frac{1}{2} G_{i0} G_{i0} + (\mathcal{D}_i \phi)^\dagger (\mathcal{D}_i \phi) \\ &+ (\mathcal{D}_0 \phi)^\dagger (\mathcal{D}_0 \phi) + \frac{\lambda}{2} (\phi^\dagger \phi - \zeta^2)^2. \end{aligned} \quad (7)$$

3 The Axially Symmetric Magnetic Ansatz

3.1 The Ansatz

The axially symmetric magnetic ansatz for the SU(2) gauge field is given by [15], [16]

$$\begin{aligned} gA_i^a &= -\frac{1}{r} \psi_1(r, \theta) \hat{n}_\phi^a \hat{\theta}_i + \frac{1}{r} \psi_2(r, \theta) \hat{n}_\theta^a \hat{\phi}_i + \frac{1}{r} R_1(r, \theta) \hat{n}_\phi^a \hat{r}_i - \frac{1}{r} R_2(r, \theta) \hat{n}_r^a \hat{\phi}_i, \\ gA_0^a &= \tau_r(r, \theta) \hat{n}_r^a + \tau_\theta(r, \theta) \hat{n}_\theta^a, \\ g\Phi^a &= \Phi_1(r, \theta) \hat{n}_r^a + \Phi_2(r, \theta) \hat{n}_\theta^a = \Phi(r, \theta) \hat{\Phi}^a, \\ \boldsymbol{\xi} &= i \begin{pmatrix} \sin \frac{\alpha(r, \theta)}{2} e^{-in\phi} \\ -\cos \frac{\alpha(r, \theta)}{2} \end{pmatrix} \\ \hat{\Phi}^a &= \boldsymbol{\xi}^\dagger \sigma^a \boldsymbol{\xi} = -\hat{h}^a. \end{aligned} \quad (8)$$

where the Higgs modulus, $g|\Phi| = \Phi = \sqrt{\Phi_1^2 + \Phi_2^2}$. The axially symmetric ansatz for the U(1) gauge field is given by

$$g' B_\mu = B_0 \delta_\mu^0 + \frac{1}{r} \mathcal{B}(r, \theta) \hat{\phi}_j \delta_\mu^j. \quad (9)$$

In the rectangular coordinate system, the unit vector, [17]

$$\begin{aligned}
\hat{h}^a &= h_1(r, \theta) \hat{n}_r^a + h_2(r, \theta) \hat{n}_\theta^a \\
&= \sin \alpha \cos n\phi \delta^{a1} + \sin \alpha \sin n\phi \delta^{a2} + \cos \alpha \delta^{a3}, \\
\cos \alpha &= \{h_1 \cos \theta - h_2 \sin \theta\}, \quad \sin \alpha = \{h_1 \sin \theta + h_2 \cos \theta\} \\
h_1 &= \cos(\alpha - \theta), \quad h_2 = \sin(\alpha - \theta), \quad \alpha = \alpha(r, \theta).
\end{aligned} \tag{10}$$

From our previous work in the SU(2) Georgi-Glashow [19], we know that for the MAC, MAP, and vortex-rings solutions, the angle $\alpha(r, \theta) \rightarrow p\theta$ as $r \rightarrow \infty$, where $p = 1, 2, 3, \dots$, is a natural number representing the number of magnetic poles (monopoles and antimonopoles) in the configuration. When p is odd, we get the MAC solutions and when p is even, we get the MAP solutions. The spatial spherical coordinate unit vectors are $\hat{r}_i = \sin \theta \cos \phi \delta_{i1} + \sin \theta \sin \phi \delta_{i2} + \cos \theta \delta_{i3}$, $\hat{\theta}_i = \cos \theta \cos \phi \delta_{i1} + \cos \theta \sin \phi \delta_{i2} - \sin \theta \delta_{i3}$, $\hat{\phi}_i = -\sin \phi \delta_{i1} + \cos \phi \delta_{i2}$, whereas the isospin coordinate unit vectors with ϕ -winding number $n = 1, 2, 3, \dots$ are given by

$$\begin{aligned}
\hat{n}_r^a &= \sin \theta \cos n\phi \delta_1^a + \sin \theta \sin n\phi \delta_2^a + \cos \theta \delta_3^a, \\
\hat{n}_\theta^a &= \cos \theta \cos n\phi \delta_1^a + \cos \theta \sin n\phi \delta_2^a - \sin \theta \delta_3^a, \\
\hat{n}_\phi^a &= -\sin n\phi \delta_1^a + \cos n\phi \delta_2^a.
\end{aligned} \tag{11}$$

3.2 The Equations of Motion

The magnetic ansatz (8) and (9) is substituted into the equations of motion (3) to (5). The equations of motion (3) reduced to the two following partial second order coupled nonlinear equations,

$$\begin{aligned}
&\partial^i \partial_i \Phi - \lambda \left(\frac{\Phi^2}{g^2} - \zeta^2 \right) \Phi + \frac{1}{4r^2} \{ (\mathcal{B} + n \csc \theta)^2 - (n - \psi_2)^2 - (R_2 - n \cot \theta)^2 \} \Phi \\
&- \frac{1}{4r^2} \left\{ \left(\psi_1 - \left(1 - \frac{\dot{h}_1}{h_2} \right) \right)^2 + \left(R_1 - \frac{r h'_1}{h_2} \right)^2 \right\} \Phi
\end{aligned} \tag{12}$$

$$\begin{aligned}
&+ \frac{1}{4} \{ A_0^2 (g_1 h_2 - g_2 h_1)^2 + [B_0 - A_0 (g_1 h_1 + g_2 h_2)]^2 \} \Phi = 0, \\
&\frac{1}{2r^2} \Phi \left\{ \cot \theta - r^2 \left(\frac{\partial^i \partial_i h_1}{h_2} - \frac{\partial^i h_1 \partial_i h_2}{h_2^2} \right) - (\dot{\psi}_1 + \cot \theta \psi_1) + (r R_1)' \right\} \\
&+ \frac{1}{r^2} \Phi \left\{ r \left(R_1 - \frac{r h'_1}{h_2} \right) (\ln \Phi)' - \left(\psi_1 - \left(1 - \frac{\dot{h}_1}{h_2} \right) \right) (\ln \Phi) \right\} \\
&+ \frac{1}{2r^2} \Phi (\mathcal{B} + n \csc \theta) (h_1 \psi_2 + h_2 R_2 - n(h_1 + h_2 \cot \theta)) \\
&+ \frac{1}{2} \Phi B_0 A_0 (g_1 h_2 - g_2 h_1) = 0.
\end{aligned} \tag{13}$$

Here “prime” and “dot” mean $\frac{\partial}{\partial r}$ and $\frac{\partial}{\partial \theta}$ respectively. The profile functions of the time component SU(2) gauge potential can be written as $\tau_r = A_0(r, \theta)g_1(r, \theta)$ and $\tau_\theta = A_0(r, \theta)g_2(r, \theta)$ where $g_1^2 + g_2^2 = 1$, and $g_1(r, \theta) \rightarrow h_1$, $g_2(r, \theta) \rightarrow h_2$ at asymptotically large r . The equations of motion (4) reduced to the six following partial second order coupled nonlinear equations,

$$\begin{aligned} & \partial^i F_{ij}^a + \epsilon^{abc} g A^{bi} F_{ij}^c + \epsilon^{abc} g A^{b0} F_{0j}^c = \\ & \frac{g}{2r} |\Phi|^2 \left\{ \left(R_1 - \frac{r h_1'}{h_2} \right) \hat{n}_\phi^a \hat{r}_j - \left(\psi_1 - \left(1 - \frac{\dot{h}_1}{h_2} \right) \right) \hat{n}_\phi^a \hat{\theta}_j \right\} \\ & + \frac{g}{2r} |\Phi|^2 \{ h_2 (R_2 - n \cot \theta) - h_1 (n - \psi_2) \} \hat{h}_\perp^a \hat{\phi}_j \\ & - \frac{g}{2r} |\Phi|^2 \{ (\mathcal{B} + n \csc \theta) + h_1 (R_2 - n \cot \theta) + h_2 (n - \psi_2) \} \hat{h}^a \hat{\phi}_j, \end{aligned} \quad (14)$$

$$\begin{aligned} & \partial^i F_{i0}^a + \epsilon^{abc} g A^{bi} F_{i0}^c = \\ & \frac{g}{2} |\Phi|^2 \left\{ [A_0 (g_1 h_1 + g_2 h_2) - B_0] \hat{h}^a + A_0 (g_2 h_1 - g_1 h_2) \hat{h}_\perp^a \right\}, \\ & \hat{h}_\perp^a = -h_2 \hat{n}_r^a + h_1 \hat{n}_\theta^a. \end{aligned} \quad (15)$$

The equations of motion (5) reduced to the two following partial second order coupled nonlinear equations,

$$\begin{aligned} & \left\{ \left(\partial^i \partial_i - \frac{1}{r^2 \sin^2 \theta} \right) \left(\frac{1}{r} (\mathcal{B} + n \csc \theta) \right) \right\} \hat{\phi}_j \\ & - \frac{g'^2}{2r} |\Phi|^2 \{ (\mathcal{B} + n \csc \theta) + (n - \psi_2) h_2 + (R_2 - n \cot \theta) h_1 \} \hat{\phi}_j = 0, \end{aligned} \quad (16)$$

$$\partial^i \partial_i B_0 - \frac{g'^2}{2} |\Phi|^2 \{ B_0 - A_0 (g_1 h_1 + g_2 h_2) \} = 0. \quad (17)$$

There are all together ten reduced electrically charged equations of motion (12)-(17). In the work here, we solved for the electrically neutral monopole configurations by setting A_0 and B_0 to zero and the total number of equations of motion is reduced to only seven equations.

3.3 The Energy

In the electrically neutral monopole configuration, the energy density (7) can be written as

$$\begin{aligned} e^2 \mathcal{E}_n &= \sin^2 \theta_W \mathcal{E}_1 + \cos^2 \theta_W \mathcal{E}_0, \quad \mathcal{E}_0 = \frac{g'^2}{4} G_{ij} G_{ij}, \\ \mathcal{E}_1 &= \frac{g^2}{4} F_{ij}^a F_{ij}^a + \partial^i \Phi \partial_i \Phi + \Phi^2 (\mathcal{D}^i \xi)^\dagger (\mathcal{D}_i \xi) + \frac{\lambda}{2} \sin^2 \theta_W (\Phi^2 - (g\zeta)^2)^2, \end{aligned} \quad (18)$$

$$\begin{aligned}
(\mathcal{D}^i \xi)^\dagger (\mathcal{D}_i \xi) &= \frac{1}{4} \partial^i \alpha \partial_i \alpha + \frac{n^2 (1 - \cos \alpha)}{2r^2 \sin^2 \theta} + \frac{n}{2} (1 - \cos \alpha) (g' B^i) \partial_i \phi \\
&+ \frac{1}{2} \{ \hat{n}_\phi^a \partial^i \alpha + n \partial^i \phi [\hat{n}_r^a \cos \theta - \hat{n}_\theta^a \sin \theta - \hat{h}^a] \} (g A_i^a) \\
&+ \frac{1}{4} (g A^{ai}) (g A_i^a) - \frac{1}{2} (g' B^i) (g A_i^a) \hat{h}^a + \frac{1}{4} (g' B^i) (g' B_i). \quad (19)
\end{aligned}$$

In Eq. (18), the energy density \mathcal{E}_0 is the U(1) part of the energy density and \mathcal{E}_1 is the part of the energy density that is regular over all space. The total energy of the MAC configurations is infinite due to \mathcal{E}_0 which is singular at the location of the monopoles. However the energy density \mathcal{E}_0 is regular over all space for the MAP configurations. Hence the MAP total energy $E = \frac{e}{4\pi} \int \mathcal{E}_n d^3x$ is finite.

3.4 The Unitary Gauge

In order to determine the electric and magnetic charge of the electromagnetic weak monopole configuration [12], the gauge potentials A_μ^a and Higgs field Φ^a of Eq. (8) are gauge transformed to $A_\mu'^a$ and $\Phi'^a = \delta_3^a$ in the unitary gauge. Using the gauge transformation,

$$\begin{aligned}
U_1 &= -i \begin{bmatrix} \cos \frac{\alpha}{2} & \sin \frac{\alpha}{2} e^{-in\phi} \\ \sin \frac{\alpha}{2} e^{in\phi} & -\cos \frac{\alpha}{2} \end{bmatrix} = \cos \frac{\Theta_1}{2} + i \hat{u}_r^a \sigma^a \sin \frac{\Theta_1}{2}, \quad (20) \\
\Theta_1 &= -\pi \quad \text{and} \quad \hat{u}_r^a = \sin \frac{\alpha}{2} \cos n\phi \delta_1^a + \sin \frac{\alpha}{2} \sin n\phi \delta_2^a + \cos \frac{\alpha}{2} \delta_3^a,
\end{aligned}$$

we obtain the transformed Higgs column unit vector and the SU(2) gauge potentials which are respectively given by

$$\begin{aligned}
\xi' &= U \xi = \begin{bmatrix} 0 \\ 1 \end{bmatrix} \\
g A_\mu'^a &= -g A_\mu^a - \frac{2}{r} \left\{ \psi_2 \sin \left(\theta - \frac{\alpha}{2} \right) + R_2 \cos \left(\theta - \frac{\alpha}{2} \right) \right\} \hat{u}_r^a \hat{\phi}_\mu \\
&- \partial_\mu \alpha \hat{u}_\phi^a - \frac{2n \sin \frac{\alpha}{2}}{r \sin \theta} \hat{u}_\theta^a \hat{\phi}_\mu \\
&+ 2 \left\{ \tau_r \cos \left(\theta - \frac{\alpha}{2} \right) - \tau_\theta \sin \left(\theta - \frac{\alpha}{2} \right) \right\} \hat{u}_r^a \delta_\mu^0, \quad (21)
\end{aligned}$$

or

$$\begin{aligned}
gA_\mu'^1 &= -\frac{1}{r} \cos n\phi \left\{ \psi_2 h_1 + R_2 h_2 - \frac{n \sin \alpha}{\sin \theta} \right\} \hat{\phi}_\mu \\
&- \frac{1}{r} \sin n\phi (\psi_1 - \partial_\theta \alpha) \hat{\theta}_\mu + \frac{1}{r} \sin n\phi (R_1 + r \partial_r \alpha) \hat{r}_\mu \\
&+ \{ \tau_r \sin(\alpha - \theta) - \tau_\theta \cos(\alpha - \theta) \} \cos n\phi \delta_\mu^0
\end{aligned} \tag{22}$$

$$\begin{aligned}
gA_\mu'^2 &= -\frac{1}{r} \sin n\phi \left\{ \psi_2 h_1 + R_2 h_2 - \frac{n \sin \alpha}{\sin \theta} \right\} \hat{\phi}_\mu \\
&+ \frac{1}{r} \cos n\phi (\psi_1 - \partial_\theta \alpha) \hat{\theta}_\mu - \frac{1}{r} \cos n\phi (R_1 + r \partial_r \alpha) \hat{r}_\mu \\
&+ \{ \tau_r \sin(\alpha - \theta) - \tau_\theta \cos(\alpha - \theta) \} \sin n\phi \delta_\mu^0
\end{aligned} \tag{23}$$

$$\begin{aligned}
gA_\mu'^3 &= \frac{1}{r} \left\{ \psi_2 h_2 - R_2 h_1 - \frac{n(1 - \cos \alpha)}{\sin \theta} \right\} \hat{\phi}_\mu \\
&+ \{ \tau_r \cos(\alpha - \theta) + \tau_\theta \sin(\alpha - \theta) \} \delta_\mu^0.
\end{aligned} \tag{24}$$

Here we note that the gauge potential $gA_\mu'^3$ (24) is actually the gauge potential that will give the 't Hooft electromagnetic field strength [3], $\hat{F}_{\mu\nu} = \hat{\Phi}^a F_{\mu\nu}^a - \frac{1}{g} \epsilon^{abc} \hat{\Phi}^a D_\mu \hat{\Phi}^b D_\nu \hat{\Phi}^c = \partial_\mu A_\nu - \partial_\nu A_\mu - \frac{1}{g} \epsilon^{abc} \hat{\Phi}^a \partial_\mu \hat{\Phi}^b \partial_\nu \hat{\Phi}^c$, where $A_\mu = \hat{\Phi}^a A_\mu^a$ and $\hat{\Phi}^a = \Phi^a/|\Phi|$ as $\hat{\Phi}'^a = \delta_3^a$. Hence we will refer to the gauge potential $gA_\mu'^3$ as the 't Hooft gauge potential.

The electromagnetic potential \mathcal{A}_μ and the neutral potential \mathcal{Z}_μ are defined as

$$\begin{aligned}
\begin{bmatrix} \mathcal{A}_\mu \\ \mathcal{Z}_\mu \end{bmatrix} &= \begin{bmatrix} \cos \theta_W & \sin \theta_W \\ -\sin \theta_W & \cos \theta_W \end{bmatrix} \begin{bmatrix} B_\mu \\ A_\mu'^3 \end{bmatrix} \\
&= \frac{1}{\sqrt{g^2 + g'^2}} \begin{bmatrix} g & g' \\ -g' & g \end{bmatrix} \begin{bmatrix} B_\mu \\ A_\mu'^3 \end{bmatrix}
\end{aligned} \tag{25}$$

where $\cos \theta_W = \frac{g}{\sqrt{g^2 + g'^2}} = \frac{e}{g'}$ and $\sin \theta_W = \frac{g'}{\sqrt{g^2 + g'^2}}$. Here θ_W is the Weinberg angle and the electric charge $e = \frac{gg'}{\sqrt{g^2 + g'^2}}$. Hence we can write the electromagnetic gauge potential and the neutral \mathcal{Z}^0 gauge potential as

$$\begin{aligned}
\mathcal{A}_\mu &= \frac{1}{\sqrt{g^2 + g'^2}} (g B_\mu + g' A_\mu'^3) \\
&= \frac{1}{e} (\cos^2 \theta_W g' B_\mu + \sin^2 \theta_W g A_\mu'^3) \\
\mathcal{Z}_\mu &= \frac{1}{\sqrt{g^2 + g'^2}} (-g' B_\mu + g A_\mu'^3) \\
&= \frac{1}{e} \cos \theta_W \sin \theta_W (-g' B_\mu + g A_\mu'^3).
\end{aligned} \tag{26}$$

4 The Results

The Weinberg-Salam equations of motion (12)-(17) are solved numerically using the Maple and MATLAB software for MAC, MAP, and vortex-ring configurations. The MAC configurations are obtained when the total number of poles along the z -axis are odd. The solutions discussed here are (i) single monopole (M), (ii) the three poles, monopole-antimonopole-monopole (MAM), and (v) the five poles (MAMAM) configurations. The MAP configurations are obtained when the total number of poles along the z -axis are even. The solutions discussed here are (i) the monopole-antimonopole pair or 1-MAP (MA) and (ii) the two monopole-antimonopole pairs or 2-MAP (MAMA) configurations. When $n = 3$, vortex-rings are formed from both the MAC and MAP configurations.

4.1 Numerical Procedure

The profile functions of the time component of the U(1) and SU(2) gauge fields, A_0 and B_0 are set to zero for the electrically neutral solutions. Hence the equations of motion Eq. (15) and (17) vanish identically and we are left with seven reduced coupled second order partial differential equations of motion, Eq. (12) - (14) and Eq. (16), to solve. We solve the numerical monopole solutions here for all space by solving for the profiles functions, ψ_1 , ψ_2 , R_1 , R_2 , Φ_1 , Φ_2 , and \mathcal{B} . The unit electric charge e and the Higgs vacuum expectation value $g\zeta$ are set to unity, that is $e = g\zeta = 1$. The Higgs field mass, $\mu = \frac{\lambda^{1/2}}{g}$ is varied from zero to six, $0 \leq \mu \leq 6$. The seven reduced equations of motion are then solved by fixing boundary conditions at small distances ($r \rightarrow 0$), large distances ($r \rightarrow \infty$), and along the z -axis at $\theta = 0$ and π .

The asymptotic solutions at large r are the self-dual solutions of the SU(2) Georgi-Glashow theory [18], [19], which determines the type of monopole configuration,

$$\begin{aligned}
\psi_1 &= \dot{\alpha}, \quad \psi_2 = n \left\{ 1 + \frac{\sin(\alpha - \theta)}{\sin \theta} (a \cos \theta + b) \right\} \\
R_1 &= 0, \quad R_2 = n \left\{ \cot \theta - \frac{\cos(\alpha - \theta)}{\sin \theta} (a \cos \theta + b) \right\} \\
\Phi_1 &= g\zeta \cos(\alpha - \theta), \quad \Phi_2 = g\zeta \sin(\alpha - \theta), \quad a, b = \text{constant}, \\
\mathcal{B} &= \mathcal{B}_G + \mathcal{B}_H \\
\mathcal{B}_G &= \psi_2 h_2 - R_2 h_1 = \frac{n((a + b) - \cos \alpha)}{\sin \theta} - \frac{na(1 - \cos \theta)}{\sin \theta} \\
\mathcal{B}_H &= -\frac{n(1 - \cos \alpha)}{\sin \theta},
\end{aligned} \tag{27}$$

where \mathcal{B}_G and \mathcal{B}_H are the Maxwell part and Dirac part of the U(1) magnetic field profile function respectively. The function $\alpha(r, \theta) = p\theta$ where p is a natural number that determines the total number of magnetic monopoles and antimonopoles in

the configurations. In the MAC configurations, the parameter p is an odd integer, $a = 1$ and $b = 0$. In the MAP configurations, the parameter p is an even integer, $a = 0$ and $b = 1$. The profile function \mathcal{B} vanishes only for the MAP solutions. We solved the equations of motion (12)-(17) when $p = 1, 2, 3, 4, 5$ and the ϕ -winding number $n = 1, 2$, and 3. Hence the U(1) gauge potential $g'B_i$ of the monopole solutions presented here approaches the 't Hooft gauge potential $gA_i'^3 = \frac{1}{r} \left\{ \psi_2 h_2 - R_2 h_1 - \frac{n(1-\cos\alpha)}{\sin\theta} \right\} \hat{\phi}_i$ at large r .

The neutral gauge potential \mathcal{Z}_μ (26) therefore vanishes as $r \rightarrow \infty$ and this neutral \mathcal{Z}^0 field carry zero net electric and net magnetic charge as expected. The electromagnetic gauge potential $\mathcal{A}_\mu \rightarrow \frac{1}{e}(g'B_\mu)$ when r goes to infinity. Since the boundary conditions for the MAC and MAP solutions are such that $\mathcal{B} \rightarrow -\frac{n(1-\cos\theta)}{\sin\theta}$ and $\mathcal{B} \rightarrow 0$ respectively at r infinity, the MAP configurations possess zero net magnetic charge whereas the MAC configurations possess magnetic charge $\frac{4\pi n}{e}$.

The electromagnetic dipole moment μ_m of the MAP configurations can also be calculated by using the boundary condition at large r ,

$$\mathcal{A}_i \rightarrow \frac{1}{e}(g'B_i) = \frac{1}{e} \left(\frac{1}{r} \mathcal{B} \hat{\phi}_i \right) = \frac{1}{e} \mathcal{B} \sin\theta \partial_i \phi = -\frac{\hat{\phi}_i}{r \sin\theta} \left(\frac{\mu_m \sin^2\theta}{r} \right). \quad (28)$$

Hence $r\mathcal{B} = -e\mu_m \sin\theta$ and by plotting the numerical result for $r\mathcal{B}$, we can read the magnetic dipole moment for the MAP solutions in unit of $\frac{1}{e}$ at $\theta = \frac{\pi}{2}$.

The asymptotic solutions at small r are the trivial vacuum solution and is a common boundary condition for all the monopole configurations,

$$\begin{aligned} \psi_1(0, \theta) = \psi_2(0, \theta) = R_1(0, \theta) = R_2(0, \theta) &= 0, \\ \sin\theta \Phi_1(0, \theta) + \cos\theta \Phi_2(0, \theta) &= 0, \\ \frac{\partial}{\partial r} \{ \cos\theta \Phi_1(r, \theta) - \sin\theta \Phi_2(r, \theta) \} \Big|_{r=0} &= 0, \\ \mathcal{B}(0, \theta) = \mathcal{B}_G(0, \theta) &= 0. \end{aligned} \quad (29)$$

The common boundary condition along the z -axis at $\theta = 0$ and π for all the monopole configurations is

$$\partial_\theta \psi_1 = \partial_\theta \psi_2 = R_1 = R_2 = \partial_\theta \Phi_1 = \Phi_2 = \mathcal{B} = \mathcal{B}_G = 0. \quad (30)$$

The monopole solutions are solved numerically using the mathematical software, Maple and MATLAB, by fixing the boundary conditions (28) - (30) when $r = 0$, $r = \infty$, $\theta = 0$, and $\theta = \pi$ [16], [18], [19]. Using the finite difference approximation method, the seven reduced equations of motion (12) - (17) are converted into a system of nonlinear equations which is then discretized onto a non-equidistant grid of size 70×60 covering the integration regions $0 \leq \bar{x} \leq 1$ and $0 \leq \theta \leq \pi$. The compactified coordinate $\bar{x} = \frac{r}{r+1}$. Upon replacing the partial derivative $\partial_r \rightarrow (1-\bar{x})^2 \partial_{\bar{x}}$ and $\frac{\partial^2}{\partial r^2} \rightarrow (1-\bar{x})^4 \frac{\partial^2}{\partial \bar{x}^2} - 2(1-\bar{x})^3 \frac{\partial}{\partial \bar{x}}$, the Jacobian sparsity pattern of the system was constructed by using Maple. The system of

nonlinear equations is then solved numerically by MATLAB using the constructed Jacobian sparsity pattern, the trust-region-reflective algorithm, and a good initial starting solution. The overall error in the numerical results is estimated at 10^{-4} .

4.2 MAC/Vortex-ring Configurations

The MAC solutions obtained are the single n -monopole ($p = 1, n = 1, 2, 3$), the $p = 3$ (MAM), and the $p = 5$ (MAMAM) configurations when the θ -winding number $n = 1$ and 2. When $p = 3, 5$ and $n = 3$, two vortex-rings with centers along the z -axis together with one monopole located at $r = 0$ are formed. The profiles functions, $\psi_1, \psi_2, R_1, R_2, \Phi_1, \Phi_2$, and \mathcal{B}_G for the MAC solutions are obtained numerically and they are all bounded functions of r and θ .

The Higgs field modulus $g|\Phi|$ for the MAC configurations are shown in Figure 1 by 3D plot and contour line plot along the x - z plane when the Higgs field mass $\mu = 1$, the Higgs expectation value $g\zeta = 1$ and $\theta_W = \frac{\pi}{4}$. Figure 1 (a) and (b) show the Higgs field modulus plots for the one monopole solutions when $n = 2$ and 3 respectively. Figure 1 (c) and (d) show the Higgs field modulus plots for the $p = 3$ MAC solutions when $n = 1$ and 3 and Figure 1 (e) and (f) show the Higgs field modulus plots for the $p = 5$ MAC solutions when $n = 1$ and 3 respectively. The locations of the magnetic monopoles and vortex-rings are read from the zeros of the Higgs field modulus and tabulated in Table 1 as $d_{(\rho,z)} = (\rho_i, \pm z_i)$ for $n = 1, 2, 3$, $\mu = g\zeta = 1$ and $\theta_W = \frac{\pi}{4}$. The Higgs field modulus for the MAC/vortex-ring configurations are almost similar to those of the SU(2) Georgi-Glashow model and there is no string or zero line of the Higgs field connecting the monopole and adjacent antimonopole.

The magnetic dipole moments μ_m for all the MAC configurations are expected to be zero and this is confirmed by the numerical results, that is $\mu_m = 0$ for both the SU(2) and U(1) magnetic fields. The U(1) magnetic field and the SU(2) 't Hooft magnetic field [3] are given by,

$$\begin{aligned} g' B_i^{U(1)} &= -\epsilon^{ijk} G_{jk} = -\epsilon^{ijk} \partial_j \{ \mathcal{B} \sin \theta \} \partial_k \phi \quad \text{and} \\ g B_i^{tHooft} &= -\epsilon^{ijk} \hat{F}_{jk} = -\epsilon^{ijk} \partial_j \{ g A_k'^3 \} \\ &= -\epsilon^{ijk} \partial_j \{ (\psi_2 h_2 - R_2 h_1) \sin \theta - n(1 - \cos \alpha) \} \partial_k \phi \end{aligned} \quad (31)$$

respectively can be shown by plotting for the respective magnetic field lines. The U(1) magnetic field lines can be shown by drawing the lines of constant $\{ \mathcal{B} \sin \theta \}$ and the SU(2) 't Hooft magnetic field lines can be shown by drawing the lines of constant $\{ (\psi_2 h_2 - R_2 h_1) \sin \theta - n(1 - \cos \alpha) \}$.

The U(1) and SU(2) 't Hooft magnetic field lines for the one monopole configurations are shown in Figure 2 for $\mu = g\zeta = 1$, $\theta_W = \frac{\pi}{4}$ and when $n = 2$ and 3 and they look almost similar. There is a one monopole in both the U(1) field and SU(2) 't Hooft field and hence in the electromagnetic field but the monopole is absent in the neutral \mathcal{Z}^0 field. Figure 3 and 4 show the U(1) and SU(2) 't Hooft magnetic field lines of the $p = 3$ MAC and $p = 5$ MAC configurations respectively

for $\mu = g\zeta = 1$, $\theta_W = \frac{\pi}{4}$ and when $n = 1, 2$, and 3 . Similar to the one monopole configurations of Figure 2, the monopoles and vortex-rings found in the SU(2) field are also found in the U(1) field and hence in the electromagnetic field. There are no monopoles or vortex-rings in the neutral \mathcal{Z}^0 field. The monopoles/antimonopoles in the electromagnetic field are Cho-Maison monopoles/antimonopoles with magnetic charges $\pm \frac{4\pi n}{e}$. The vortex-rings however possess zero net magnetic charge.

Similar to the $p = 3$ MAC and $p = 5$ MAC configurations of the SU(2) Georgi-Glashow model when the θ -winding number $n = 3$, a single n -monopole located at $r = 0$ and two vortex-rings with center located along the z -axis ($\pm z_i$) and radius ρ_i are formed [15]. In the MAC configurations, the monopoles and vortex-rings are found only in the electromagnetic gauge field, there is no monopole or vortex-ring present in the neutral \mathcal{Z}^0 gauge field.

The separation distance D_{z1} of the monopole/antimonopole located at $r = 0$ with the adjacent antimonopole/monopole, the separation distance D_{z2} of the chain's outer monopole/antimonopole with the adjacent antimonopole/monopole, the separation distance D_z of the two vortex-rings along the z -axis, and the diameter D_ρ of the vortex-ring, are also plotted versus μ for $0 \leq \mu^2 \leq 40$ when $g\zeta = 1$ and $\theta_W = \frac{\pi}{4}$. The graphs are shown in Figure 5 (a) and (b) when $n = 1$ and 3 respectively for the $p = 3$ and $p = 5$ MAC configurations. The graphs show that D_{z1} , D_{z2} , D_z and D_ρ become constant when $\mu > 2$. Hence the separations of monopoles, antimonopoles, and vortex-rings do not change much at large Higgs mass.

The total energy of the MAC configurations is infinite due to the presence of point magnetic charges in the U(1) field. The energy density \mathcal{E}_0 blows up at the locations of the point magnetic charge in the U(1) field. Hence the mass of these monopoles can only be estimated to be about 4 to 7 TeV as was done for the one monopole solution when $n = 1$ in Ref. [13].

$d_{(\rho,z)}$	$n = 1$	$n = 2$	$n = 3$
$p = 3$	$(0, 0), (0, \pm 3.375)$	$(0, 0), (0, \pm 2.236)$	$(0, 0), (1.424, \pm 1.283)$
$p = 5$	$(0, 0), (0, \pm 3.559),$ $(0, \pm 6.737)$	$(0, 0), (0, \pm 2.561),$ $(0, \pm 4.914)$	$(0, 0),$ $(1.690, \pm 2.928)$
$d_{(\rho,z)}$	$n = 1$	$n = 2$	$n = 3$
$p = 2$	$(0, \pm 2.202)$	$(0, \pm 1.063)$	$(1.692, 0)$
$p = 4$	$(0, \pm 1.581),$ $(0, \pm 5.435)$	$(0, \pm 1.251),$ $(0, \pm 3.166)$	$(1.606, \pm 1.693)$

Table 1: Table of monopole's and vortex-ring's positions, $d_{(\rho,z)} = (\rho_i, \pm z_i)$, when $\mu = g\zeta = 1$ and $\theta_W = \frac{\pi}{4}$.

4.3 MAP/Vortex-ring Configurations

The MAP solutions obtained are the 1-MAP ($p = 2$) and the 2-MAP ($p = 4$) configurations when the θ -winding number $n = 1$ and 2. When $n = 3$, one vortex-ring is formed in the 1-MAP configuration and two vortex-rings are formed in the 2-MAP configuration just as in the SU(2) Georgi-Glashow model [15]. As in Section 4.2, the profiles functions, ψ_1 , ψ_2 , R_1 , R_2 , Φ_1 , Φ_2 , and \mathcal{B} for the MAP solutions are obtained numerically and they are all bounded functions of r and θ .

The 3D and contour line plots of the Higgs field modulus $g|\Phi|$ along the x - z plane for the $p = 2$ and $p = 4$ MAP configurations are shown in Figure 6 for $n = 1, 2, 3$, $\mu = g\zeta = 1$ and $\theta_W = \frac{\pi}{4}$. The locations $d_{(\rho,z)} = (\rho_i, \pm z)$ of the magnetic monopoles and vortex-rings are read from the zeros of the Higgs field modulus and tabulated in Table 1 for the $p = 2$ and $p = 4$ MAP configurations when $n = 1, 2$, and 3. There is however a major difference in the Higgs field modulus here compared to the corresponding MAP solutions of the SU(2) Georgi-Glashow model. The Higgs field modulus is not only zero at the locations of the magnetic monopoles but also vanishes along a line of finite thickness connecting the monopole to the antimonopole of the pair. These observations are not surprising as they are in line with the theoretical predictions of Nambu [5] and the work of others [6] - [9].

The separations of the monopole and antimonopole D_{z1} , D_{z2} , the separation of the vortex-rings along the z -axis D_z and the diameter of the vortex-ring D_ρ are also noted and plotted versus μ for 1-MAP and 2-MAP configurations for $\mu = g\zeta = 1$, $\theta_W = \frac{\pi}{4}$ and when $n = 1$ and 3 in Figure 5 (c) and (d) respectively. Similar to the MAC configurations in Section 4.2, D_{z1} , D_{z2} , D_z and D_ρ become constant when $\mu > 2$.

The magnetic field lines of the Abelian U(1) field, the SU(2) 't Hooft field, the neutral \mathcal{Z}^0 field, and the electromagnetic field when $\mu = g\zeta = 1$ and the Weinberg angle $\theta_W = \frac{\pi}{4}$ are shown in Figure 7 and 8 for the 1-MAP configuration when $n = 1$ and 3 respectively and in Figure 9 and 10 for the 2-MAP configuration when $n = 1$ and 3 respectively. Unlike the MAC configurations, there is no monopole or vortex-ring found in the Abelian U(1) field. The monopole and antimonopole pairs and vortex-rings are found only in the SU(2) gauge field. From Eq. (26), the monopole/antimonopole possess fractional magnetic charge $\pm \frac{4\pi}{e} \sin^2 \theta_W$ in the electromagnetic gauge field and they possess fractional magnetic charge $\pm \frac{4\pi}{e} \sin \theta_W \cos \theta_W$ in the neutral \mathcal{Z}^0 field. Hence $\cos \theta_W = \sin \theta_W = \frac{1}{\sqrt{2}}$ and the Weinberg angle can only take one non trivial value of $\theta_W = \frac{\pi}{4}$. The monopole/antimonopole then possess magnetic charge $\pm \frac{2\pi}{e}$ which is half the magnetic charge of a Cho-Maison monopole.

The SU(2) 't Hooft magnetic field lines of the 1-MAP configuration resemble the magnetic field lines of a bar magnet and those of the 2-MAP configuration resemble the magnetic field lines of two bar magnets. In the U(1) gauge field, there is totally no magnetic monopole or vortex-ring but only the magnetic flux of electric current loops. However, the U(1) magnetic field possesses similar magnetic

dipole moment μ_m as the SU(2) 't Hooft magnetic field as $g'B_i \rightarrow gA_i^3$ at large r . In the SU(2) 't Hooft magnetic field, the magnetic dipole moment is due to the monopole-antimonopole pair but there is no monopole-antimonopole pair in the U(1) magnetic field, hence in the U(1) field, the magnetic dipole moment must have come from external delta function electric current loops. There is at least one such current loop in the 1-MAP configurations (Figure 7 and 8) and the 2-MAP vortex-rings configuration (Figure 10), and two such current loops in the 2-MAP configuration when $n = 1$ (Figure 9).

The magnetic dipole moments μ_m in unit of $\frac{1}{e}$ for all the MAP configurations are calculated numerically [16], [20] and the results μ_{mn} are tabulated in Table 2 for the 1-MAP ($n = 1, 3$) and 2-MAP ($n = 1, 3$) configurations for $0 \leq \mu^2 \leq 40$. The magnetic dipole moment μ_{mn} which is the magnetic dipole moment μ_m of the configuration per n and per MAP is plotted versus μ for the 1-MAP and 2-MAP configurations when $g\zeta = 1$, $\theta_W = \frac{\pi}{4}$ and $n = 1$ and 3 in Figure 5 (e). The graphs of μ_{mn} decrease exponentially fast with increasing μ and the magnetic dipole moments are only additive for a small range of $0.1 < \mu < 0.8$ when the μ_{mn} of the 1-MAP ($n = 1, 3$) and 2-MAP ($n = 1$) are almost the same.

The total energy of the MAP configurations is finite due to the fact that there is no point magnetic charge presence in the U(1) field. The total energy E_n in unit of $4\pi e$ which is the energy per n per MAP of the configurations is tabulated in Table 2 for the 1-MAP ($n = 1, 3$) and 2-MAP ($n = 1, 3$) configurations for $0 \leq \mu^2 \leq 40$ and also plotted versus μ as shown in Figure 5 (f) when $g\zeta = 1$ and $\theta_W = \frac{\pi}{4}$. We find that the energy $E_n(\frac{p}{2}, n)$ increases approximately linearly with μ when $\mu > 2$. We also notice that the ratio of the energy is such that $\frac{E_n(\frac{p}{2}, 3)}{E_n(\frac{p}{2}, 1)} < 1$ when $0 \leq \mu \leq 6$ which is consistent with theory.

4.4 The Baryon Number

Since the MAP and vortex-rings solutions of Section 4.3 possess finite energy and zero net topological magnetic charge, the baryon number of these configurations can be calculated using the definition of Ref. [7],

$$Q_B = \frac{g^2}{32\pi^2} \int_{t=t_0} d^3 K^0, \quad K^0 = \epsilon^{ijk} \left(F_{ij}^a A_k^a - \frac{1}{3} g \epsilon_{abc} A_i^a A_j^b A_k^c \right). \quad (32)$$

The SU(2) gauge potential (8) is then gauge transformed into the correct gauge by using the gauge transformation,

$$\begin{aligned} U_2 &= \cos \left(\frac{\Theta_2(r)}{2} \right) + i \hat{u}_r^a \sin \left(\frac{\Theta_2(r)}{2} \right), \quad \Theta_2(0) = 0 \text{ and } \Theta_2(r)|_{r \rightarrow \infty} = -\pi, \\ \hat{u}_r^a &= \sin \left(\frac{p\theta}{2} \right) \cos n\phi \delta_1^a + \sin \left(\frac{p\theta}{2} \right) \sin n\phi \delta_2^a + \cos \left(\frac{p\theta}{2} \right) \delta_3^a, \end{aligned} \quad (33)$$

where the number of poles p is an even number for the MAP configurations. The gauge transformation U_2 rotates the Higgs field direction $\hat{\Phi}^a$ to δ_3^a as $r \rightarrow \infty$ but

1-MAP (n=1)											
μ^2	0	0.05	0.1	0.5	1	4	8	10	20	30	40
E_n	1.186	1.306	1.3527	1.581	1.751	2.317	2.734	2.905	3.572	4.088	4.520
μ_{mn}	1.844	1.572	1.514	1.389	1.339	1.274	1.244	1.236	1.214	1.203	1.196
1-MAP (n=3)											
μ^2	0	0.05	0.1	0.5	1	4	8	10	20	30	40
E_n	1.067	1.118	1.137	1.318	1.418	1.685	1.856	1.920	2.155	2.329	2.476
μ_{mn}	1.679	1.574	1.547	1.380	1.309	1.214	1.183	1.176	1.171	1.168	1.167
2-MAP (n=1)											
μ^2	0	0.05	0.1	0.5	1	4	8	10	20	30	40
E_n	1.145	1.271	1.310	1.480	1.650	2.444	2.932	3.155	4.000	4.702	5.386
μ_{mn}	1.801	1.525	1.483	1.384	1.358	1.340	1.322	1.318	1.305	1.300	1.296
2-MAP (n=3)											
μ^2	0	0.05	0.1	0.5	1	4	8	10	20	30	40
E_n	1.009	1.086	1.102	1.310	1.453	1.772	2.012	2.102	2.459	2.746	3.000
μ_{mn}	1.791	1.615	1.586	1.517	1.473	1.414	1.401	1.400	1.396	1.395	1.394

Table 2: Table of values of E_n (total energy per n per MAP) and μ_{mn} (magnetic dipole moment per n per MAP) for the 1-MAP ($n = 1, n = 3$) and 2-MAP ($n = 1, n = 3$) configurations at various values of $0 \leq \mu^2 \leq 40$. Here $\theta_W = \frac{\pi}{4}$.

leaves the Higgs direction unrotated at the origin $r = 0$. The baryon number (32) calculated from the gauge transformed potential will give

$$Q_B = \frac{n}{4}(1 - (-1)^{p/2}), \quad p = \text{even number.} \quad (34)$$

Hence the baryon number for the 1-MAP configurations is $Q_B = \frac{n}{2}$ and the baryon number for the 2-MAP configurations is $Q_B = 0$. Therefore the 1-MAP configuration is a sphaleron and the 2-MAP configuration is a sphaleron and an anti-sphaleron.

From our numerical results, we have confirmed that sphaleron is made up of a monopole-antimonopole pair with an electromagnetic current loop circulating around the dipole. The Weinberg angle is $\theta_W = \frac{\pi}{4}$ and the monopole and antimonopole charges are $\pm \frac{2\pi}{e}$ respectively which is half the magnetic charge of a Cho-Maison monopole. The U(1) field carries an external electric current loop which contributes to the magnetic dipole moment μ_m of the U(1) field whereas the SU(2) 't Hooft field carries the monopole-antimonopole pair which contributes the same magnetic dipole moment μ_m as the U(1) field. The monopole and anti-monopole in the MAP configuration is held by the neutral \mathcal{Z}^0 flux string.

5 Comments

In summary, we have shown that by just using the axially symmetric magnetic ansatz (8), we are able to solve numerically for the MAP (sphaleron) configurations when the parameter p is an even number and the MAC (Cho-Maison monopole) configurations when p is an odd number although the numerical accuracies of the solutions will decrease with increasing value of parameter p and θ -winding number n .

Our results for the MAP configurations are in line with results of Nambu [5] and others [6] - [9]. Our 1-MAP configuration is a sphaleron with finite energy and baryon number $\frac{1}{2}$ and that within the sphaleron there is monopole-antimonopole pair together with a loop of electromagnetic current circulating the dipole. The U(1) field carries the electric current loop and the SU(2) 't Hooft field carries the monopole-antimonopole pair [6] - [9]. The monopole-antimonopole pair is also bounded by a flux string of the neutral \mathcal{Z}^0 field [5] - [9]. We found that the Weinberg angle can only take value of $\theta_W = \frac{\pi}{4}$ and the monopole and antimonopole are actually half Cho-Maison monopole with magnetic charges $\pm \frac{2\pi}{e}$ respectively. This also implies that magnetic dipole moment of the sphaleron μ_m is contributed equally by both the monopole-antimonopole pair and the electromagnetic current loop and not 70% and 30% respectively as mentioned in Ref. [8]. We also found that the 2-MAP configuration is a sphaleron-antisphaleron pair with baryon number $Q_B = 0$.

In Ref. [10] and [11], sphalerons, antisphalerons, and vortex-rings configurations are shown to exist in the SU(2)×U(1) Weinberg-Salam theory by using the same magnetic ansatz (8) for the SU(2) gauge field but different Higgs field profile functions. However their numerical results do not reveal the inner structure of the sphaleron. The sphaleron and the sphaleron-antisphaleron pair obtained are just a point particle and a two point particles respectively along the z -axis when $n = 1$ and 2 and they possess magnetic dipole moment. Hence their results failed to explain the origin of the magnetic dipole moment of the sphaleron. When $n = 3$, their one multisphaleron does not give a vortex-ring configuration and their sphaleron-antisphaleron pair becomes a vortex-ring. These results for vortex-ring are different from our results as our one sphaleron (1-MAP) gives rise to a vortex-ring and our sphaleron-antisphaleron pair (2-MAP) gives rise to two vortex-rings configurations when $n = 3$.

From the numerical results of Ref. [10], it was given that when $n = 1$, the ratios of the magnetic dipole moment $\mu_{(m,n)}$ is $\frac{\mu_{(2,1)}}{\mu_{(1,1)}}|_{\lambda=1} \approx 2.0$. They also state that $\frac{\mu_{(m,1)}(\lambda=1)}{\mu_{(m,1)}(\lambda=0)} \approx 0.75$ where $m = 1$ and 2. Our numerical results for magnetic dipole moment $\mu_m(\frac{p}{2}, n)$ of the 1-MAP and 2-MAP solutions also give almost the same ratios as that of Ref. [10], where the ratios $\frac{\mu_m(2,1)}{\mu_m(1,1)}|_{\lambda=0} = 1.953$, $\frac{\mu_m(2,1)}{\mu_m(1,1)}|_{\lambda=1} = 1.993$, $\frac{\mu_m(1,1,\lambda=1)}{\mu_m(1,1,\lambda=0)} = 0.753$ and $\frac{\mu_m(2,1,\lambda=1)}{\mu_m(2,1,\lambda=0)} = 0.768$.

Again by comparing the ratio of the energy of the sphaleron of Ref. [10] at $\lambda = 1$, where $\frac{E_{(2,1)}}{E_{(1,1)}}|_{\lambda=1} = 1.997 \pm 0.003$ with the ratio of the energy of our MAP

configurations, $\frac{E(2,1)}{E(1,1)}|_{\lambda=1} = 1.872$, we found that the results are almost the same. Hence their sphaleron may corresponds to our 1-MAP configuration and their sphaleron-antisphaleron pair may corresponds to our 2-MAP configuration.

The MAC configurations are different from the MAP configurations as the monopoles and antimonopoles in the MAC configurations are all whole Cho-Maison monopoles and antimonopoles with magnetic charges $\pm \frac{4\pi}{e}$ respectively. There is no flux string joining a monopole and its adjacent antimonopole. The U(1) field carries the monopoles and antimonopoles /vortex-rings and the U(1) part of the energy is infinite. The Weinberg angle can take values $0 \leq \theta_W \leq \frac{\pi}{2}$. Our MAC configurations include the one Cho-Maison monopole solution of Ref. [12]. Although the MAC configurations possess infinite energy, the mass of the monopole can be estimated as was done for the one monopole in Ref. [13] to be about 4 to 7 TeV. Hence by using the axially symmetric magnetic ansatz (8), we are able to solve numerically for the whole family of MAC configurations although the numerical accuracy of the solutions will decrease with increasing value of odd number of p .

Years ago, Coleman [23] had noted that there is no unique way of representing the electromagnetic field in the region outside the Higgs vacuum at finite value of r . One proposal was given by 't Hooft as in equation (31) and another was given in equation (4) of Ref. [8]. In our work here, we prefer the definition of 't Hooft as the numerical results obtained for the U(1) gauge potential is very close to the 't Hooft gauge potential that is $g'B_i \approx gA_i^3$ not only at $r \rightarrow \infty$ but for all space for the $n = 1$ MAC configurations. Hence the neutral \mathcal{Z}^0 field is almost zero and the electromagnetic field is almost independent of the Weinberg angle $0 \leq \theta_W \leq \frac{\pi}{2}$.

The MAP and MAC configurations studied here are electrically neutral. Hence further work are done by introducing electric charges into these configurations. This is done by letting the time component of the gauge field functions, A_0 and B_0 of the magnetic ansatz (8) and (9) to be nonvanishing. This work on the MAC, MAP and vortex-ring dyons of the SU(2) \times U(1) Weinberg-Salam model will be reported in the near future.

Further investigation of the MAP (sphaleron) configurations are also carried out for large values of Higgs self-coupling constant λ by looking for higher energy branches of the solutions other than the fundamental branch which exist for all values of $\lambda \geq 0$ as was done for the MAP [21] and MAC [22] solutions of the SU(2) Georgi-Glashow model. Similar bifurcations and transitions of higher energy branches of solutions may also occur in the Weinberg-Salam model. These investigations will be reported in a later work.

We conclude that the MAP, MAC, and vortex-rings solutions can exist both in the SU(2) Georgi-Glashow model as well as in the SU(2) \times U(1) Weinberg-Salam model. In the Georgi-Glashow model they all possess finite energy and in the Weinberg-Salam model only the MAP/vortex-rings configurations with zero net magnetic charge possess finite energy. In fact the 1-MAP configuration in the Weinberg-Salam model is a sphaleron and the 2-MAP is a sphaleron-antisphaleron pair. Another monopole configuration that can exist both in the Georgi-Glashow

model [20], [24], [25] and the Weinberg-Salam model [26] is the half-monopole configuration. The half-monopole configuration in the SU(2) Georgi-Glashow model upon symmetry breaking to the U(1) group possesses finite energy [24], [25]. We have found that the half-monopole configuration in the SU(2) \times U(1) Weinberg-Salam model also possesses finite energy [26] and this work will be reported soon.

Acknowledgements

The authors would like to thank the Ministry of Science, Technology and Innovation for the ScienceFund Grant (account number: 305/PFIZIK/613613) and the Ministry of Higher Education for the Fundamental Research Grant Scheme (FRGS).

References

- [1] P.A.M. Dirac, Pro. Royal London Soc. Series **A** **133**, 60 (1931); Phys. Rev. **74**, 817 (1948).
- [2] T.T. Wu and C.N. Yang, *Properties of Matter under Unusual Conditions*, edited by H. Mark and S. Fernbach (Wiley, New York, 1969) 349; Nucl. Phys. **B** **107**, 365 (1976); Phys. Rev. **D** **16**, 1018 (1977).
- [3] G. 't Hooft, Nucl. Phys. **B79**, 276 (1974); A.M. Polyakov, JETP Lett. **20**, 194 (1974).
- [4] J. Beringer et al. (Particle Data Group), Phys. Rev. **D** **86**, 010001 (2012).
- [5] Y. Nambu, Nucl. Phys. **B** **130**, 505 (1977); Int. J. Theor. Phys. **17** (1978) 287.
- [6] A. Achucarro and T. Vachaspati, Phys. Rep. **327**, 347 (2000).
- [7] F.R. Klinkhamer and N.S. Manton, Phys. Rev. **D** **30**, 2212 (1984).
- [8] M. Hindmarsh and M. James, Phys. Rev. **D** **49**, 6109 (1994).
- [9] E. Radu and M.S. Volkov, Phys. Rev. **D** **79**, 025003 (2009).
- [10] B. Kleihaus, J. Kunz, and M. Leißner, Phys. Lett. **B663**, 438 (2008); Phys. Lett. **B678**, 313 (2009).
- [11] R. Ibadov, B. Kleihaus, J. Kunz, and M. Leißner, Phys. Lett. **B686**, 298 (2010); Phys. Rev. **D82**, 125037 (2010).
- [12] Y.M. Cho and D. Maison, Phys. Lett. **B391**, 360 (1997).

- [13] Y.M. Cho, Kyoungtae Kimm, and J.H. Yoon, *Finite Energy Electroweak Dyon*, hep-ph/1305.1699v1 (2013); *Mass of the Electroweak Monopole*, hep-ph/1212.3885v5 (2013).
- [14] J. Pinfold, Rad. Meas. **44**, 834 (2009); CERN Courier **52**, No. 7, p. 10 (2012).
- [15] B. Kleihaus and J. Kunz, Phys. Rev. **D 61**, 025003 (1999); B. Kleihaus, J. Kunz, and Y. Shnir, Phys. Lett. **B570**, 237 (2003); Phys. Rev. **D 68**, 101701 (2003); Phys. Rev. **D 70**, 065010 (2004); J. Kunz, U. Neemann and Y. Shnir, Phys. Lett. **B640**, 57 (2006).
- [16] K.G. Lim, Rosy Teh and K.M. Wong, J. Phys. G: Nucl. Part. Phys. **39** (2012) 025002.
- [17] Rosy Teh, B.L. Ng, and K.M. Wong, Int. J. Mod. Phys. **A28**, 1350144 (2013).
- [18] Rosy Teh, K.M. Wong and K.G. Lim, Int. J. Mod. Phys. **A25**, 5731 (2010).
- [19] Rosy Teh, P.Y. Tan, and K.M. Wong, Int. J. Mod. Phys. **A27**, 1250148, (2012).
- [20] Rosy Teh, B.L. Ng, and K.M. Wong, J. Phys. G: Nucl. Part. Phys. **40**, 035004 (2013).
- [21] Rosy Teh, Amin Soltanian, and K.M. Wong, Phys. Rev. **D89**, 045018 (2014).
- [22] J. Kunz, U. Neemann, and Y. Shnir, Phys. Lett. **B640**, 57 (2006).
- [23] Coleman S 1975 New Phenomena in Subnuclear Physics: Proc. 1975 Int. School of Physics Ettore Majorana ed A Zichichi (New York: Plenum) p 297.
- [24] Rosy Teh, B.L. Ng, and K.M. Wong, Mod. Phys. Letts. **A27**, 1250233 (2012).
- [25] Rosy Teh, B.L. Ng, and K.M. Wong, Annals of Physics **343C**, 1 (2014).
- [26] Rosy Teh, B.L. Ng, and K.M. Wong, *Half-Monopole in the Weinberg-Salam Model*, invited oral paper to be presented in the “The 8th Joint Meeting of Chinese Physicists Worldwide (OCPA8): Looking Forward to Quantum Frontiers and Beyond International Conference on Physics and Education, Singapore (23-27 June 2014)”.

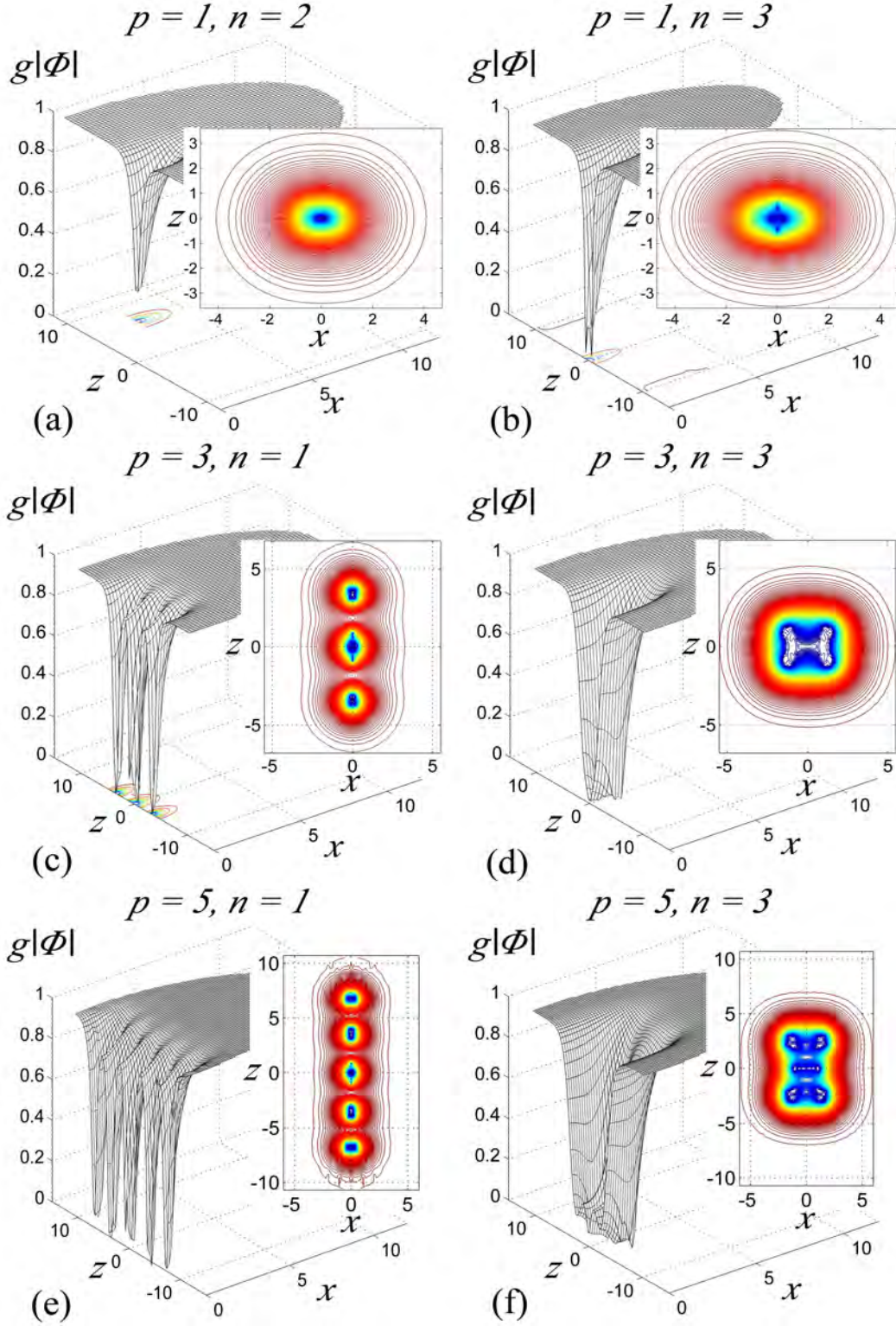


Figure 1: 3D and contour line plot of the Higgs field modulus $g|\Phi|$ along the x - z plane for the one monopole solutions when (a) $n = 2$ and (b) $n = 3$, for the $p = 3$ MAC solutions when (c) $n = 1$ and (d) $n = 3$, and for the $p = 5$ MAC solutions when (e) $n = 1$ and (f) $n = 3$. Here $\mu = g\zeta = 1$ and $\theta_W = \frac{\pi}{4}$.

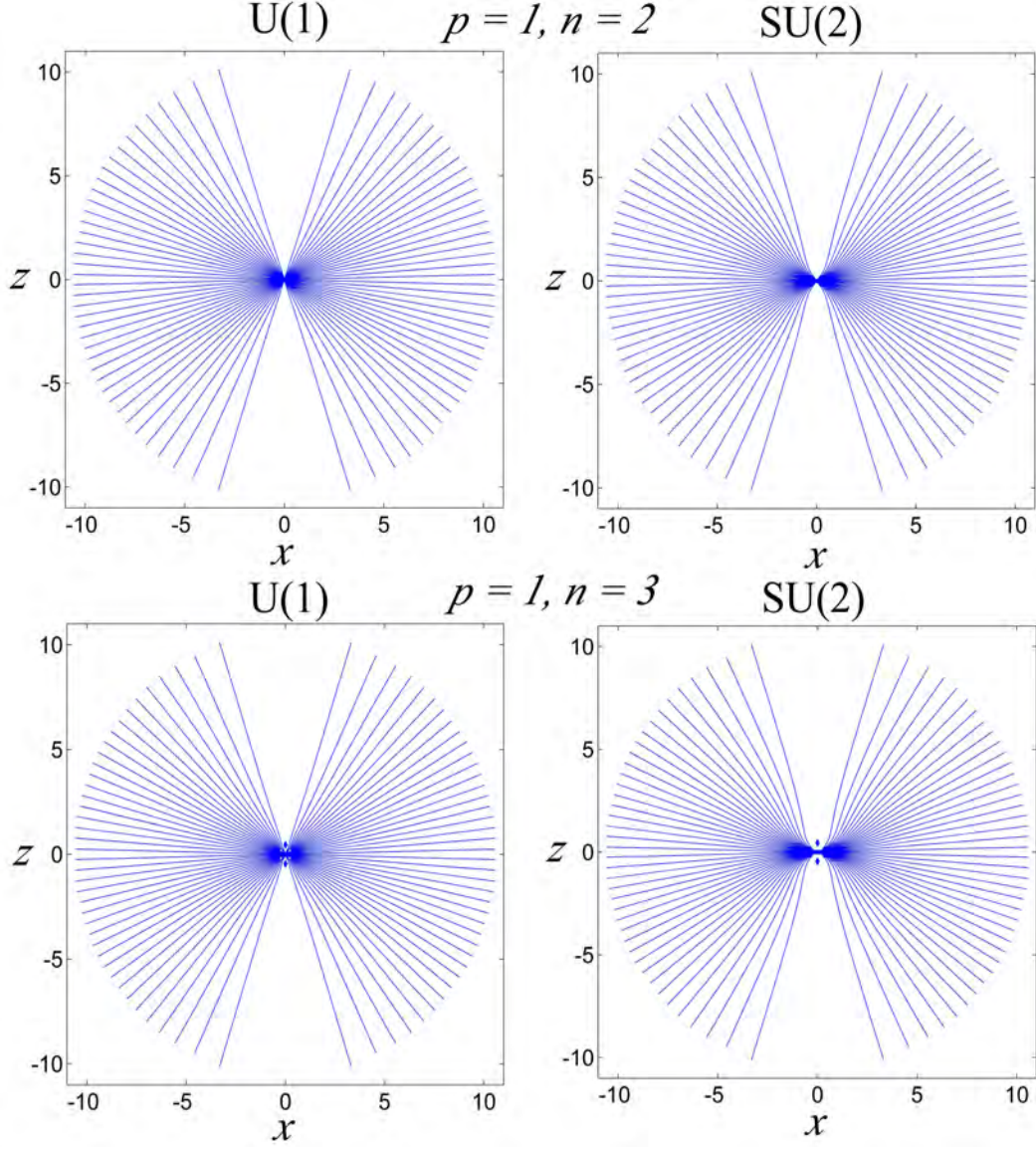


Figure 2: The contour line plot of the U(1) and SU(2) 't Hooft magnetic field lines for the one monopole configurations along the x - z plane when $n = 2$ and 3. Here $\mu = g\zeta = 1$ and $\theta_W = \frac{\pi}{4}$.

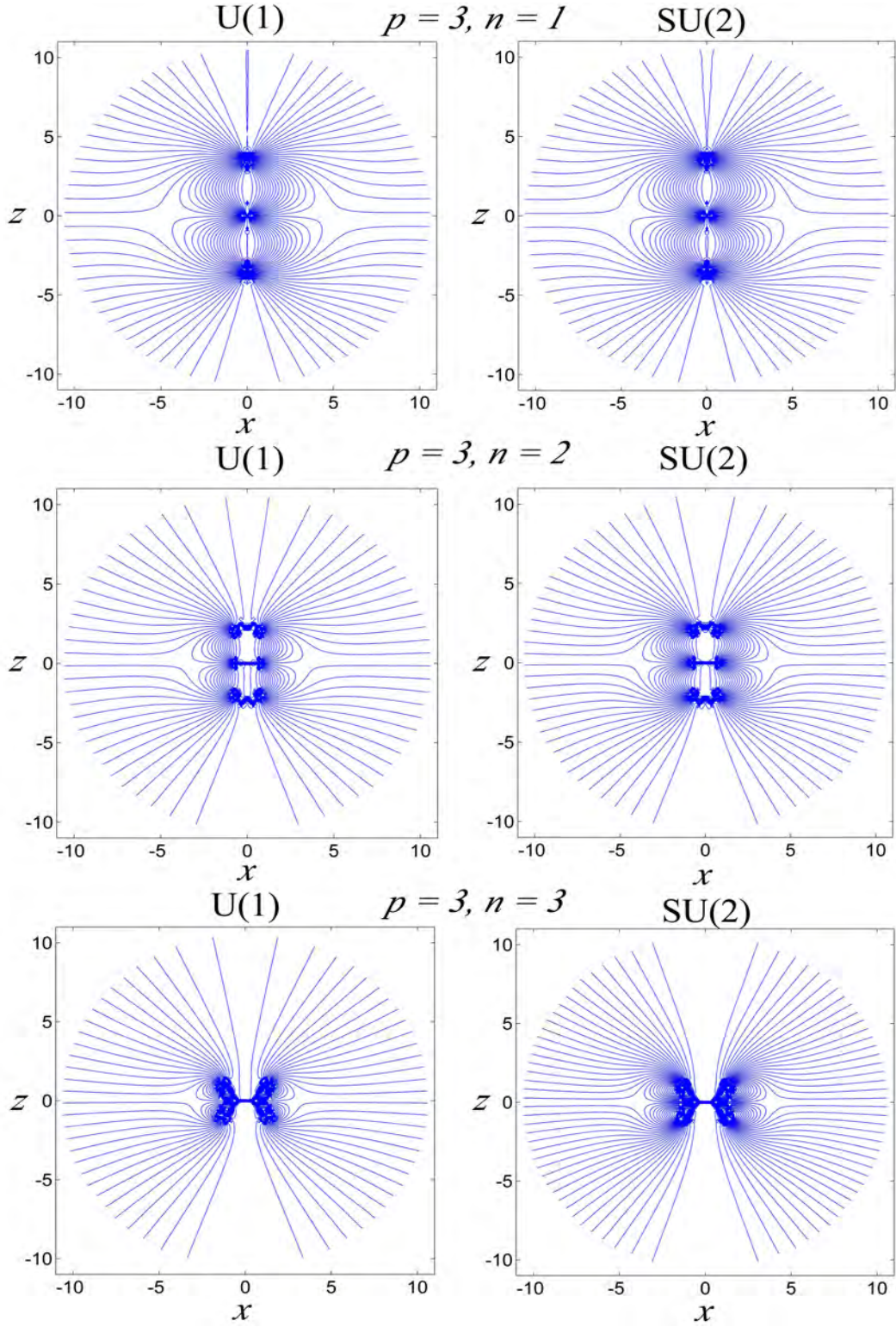


Figure 3: The contour line plot of the U(1) and SU(2) 't Hooft magnetic field lines for the $p = 3$ MAC configurations along the x - z plane when $n = 1, 2$ and 3 . Here $\mu = g\zeta = 1$ and $\theta_W = \frac{\pi}{4}$.

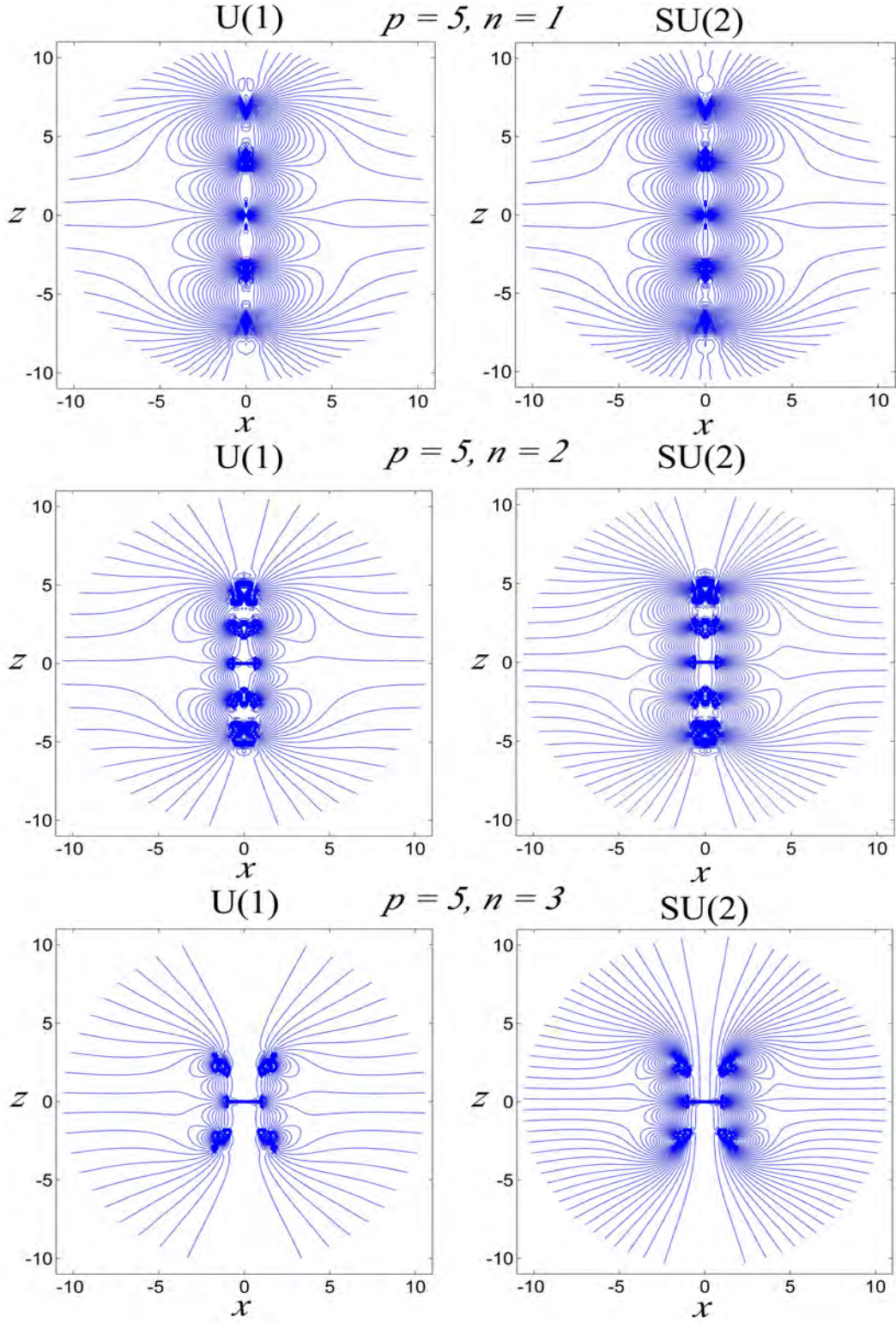


Figure 4: The contour line plot of the U(1) and SU(2) 't Hooft magnetic field lines for the $p = 5$ MAC configurations along the x - z plane when $n = 1, 2$ and 3 . Here $\mu = g\zeta = 1$ and $\theta_W = \frac{\pi}{4}$.

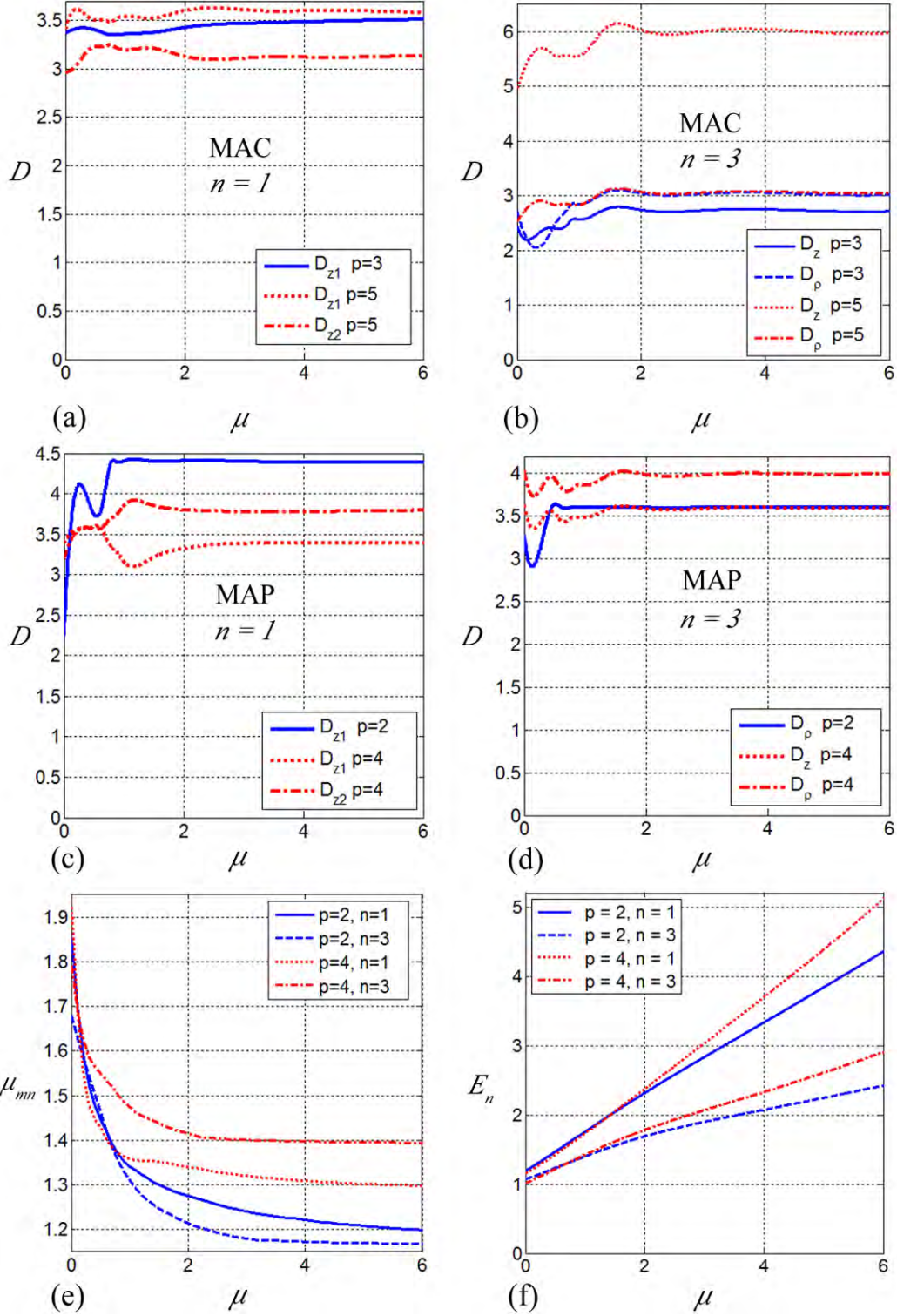


Figure 5: The graphs of D_{z1} and D_{z2} versus μ when (a) $n = 1$ and (b) $n = 3$, for the $p = 3, 5$, MAC configurations and when (c) $n = 1$ and (d) $n = 3$, for the $p = 2, 4$, MAP configurations. (e) The graphs of magnetic dipole moment μ_{mn} versus μ when $n = 1, 3$ for the MAP configurations. (f) The graphs of energy E_n versus μ when $n = 1, 3$ for the MAP configurations. Here $g\zeta = 1$ and $\theta_W = \frac{\pi}{4}$.

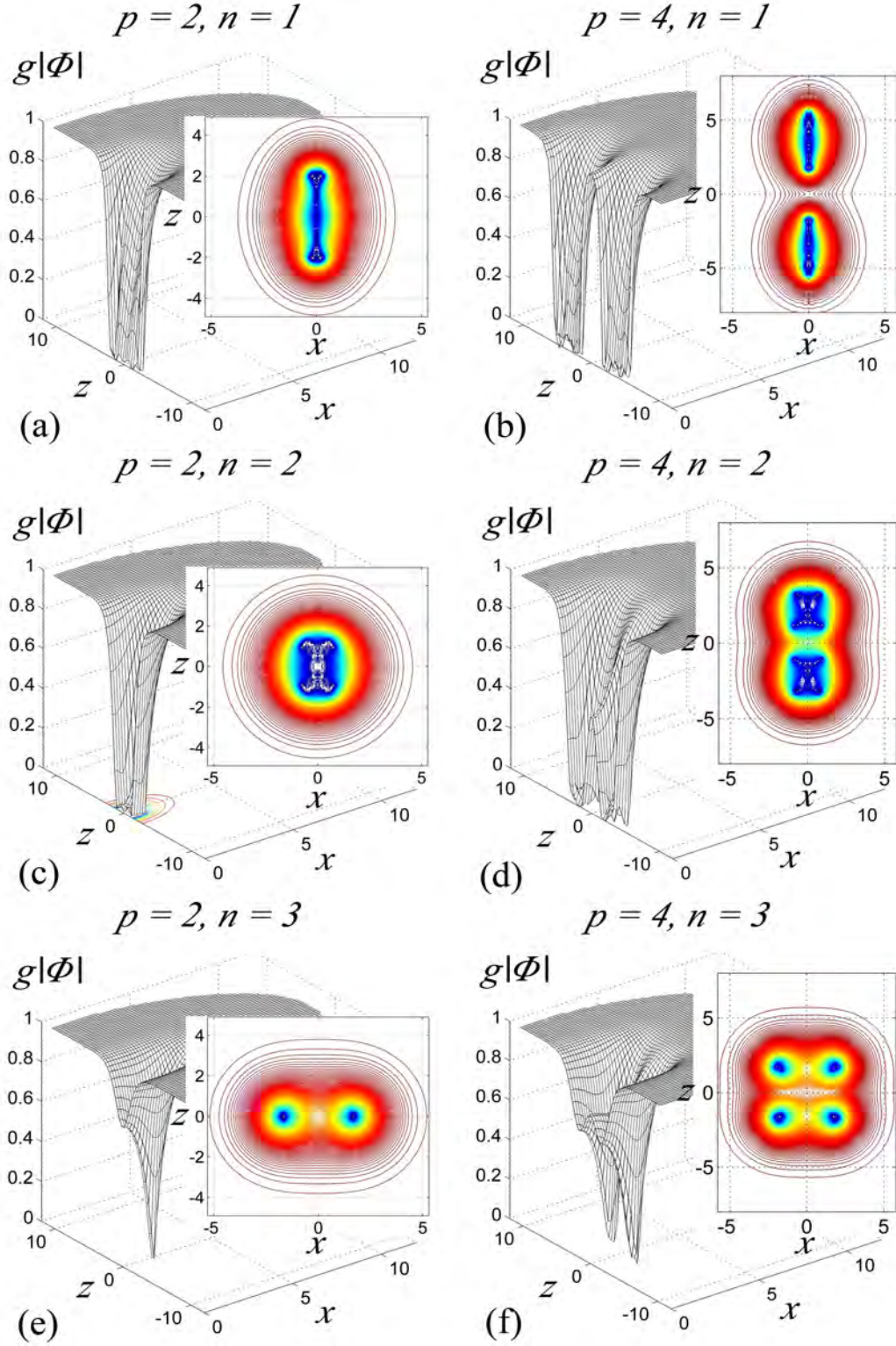


Figure 6: The 3D and contour line plots of the Higgs field modulus $g|\Phi|$ along the x - z plane for the MAP configurations when (a) $p = 2, n = 1$, (b) $p = 4, n = 1$, (c) $p = 2, n = 2$, (d) $p = 4, n = 2$, (e) $p = 2, n = 3$, and (f) $p = 4, n = 3$. Here $\mu = g\zeta = 1$ and $\theta_W = \frac{\pi}{4}$.

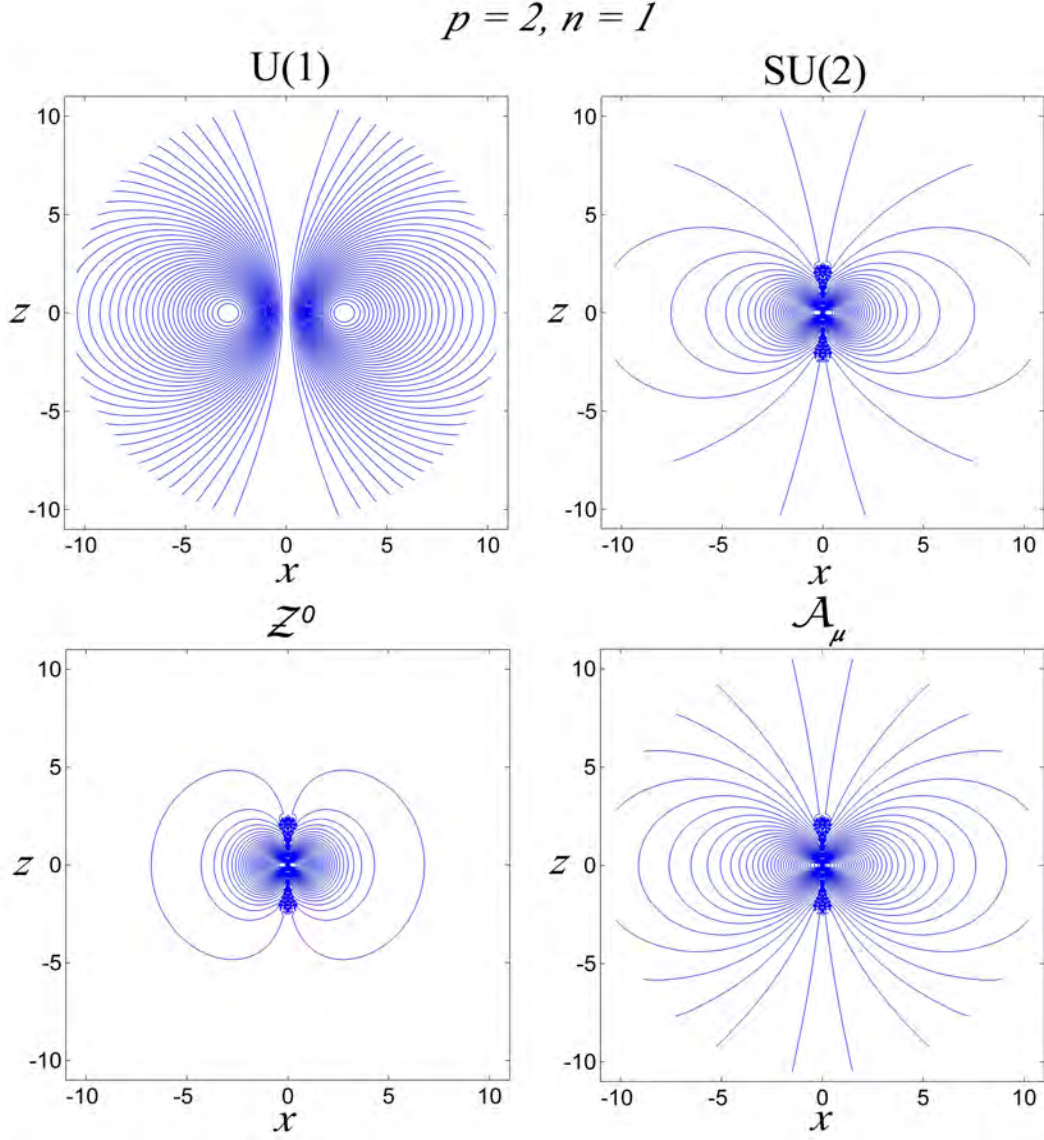


Figure 7: The contour line plot of the U(1), SU(2) 't Hooft, neutral \mathcal{Z}^0 , and electromagnetic field lines for the 1-MAP configuration along the x - z plane when $p = 2, n = 1$. Here $\mu = g\zeta = 1$ and $\theta_W = \frac{\pi}{4}$.

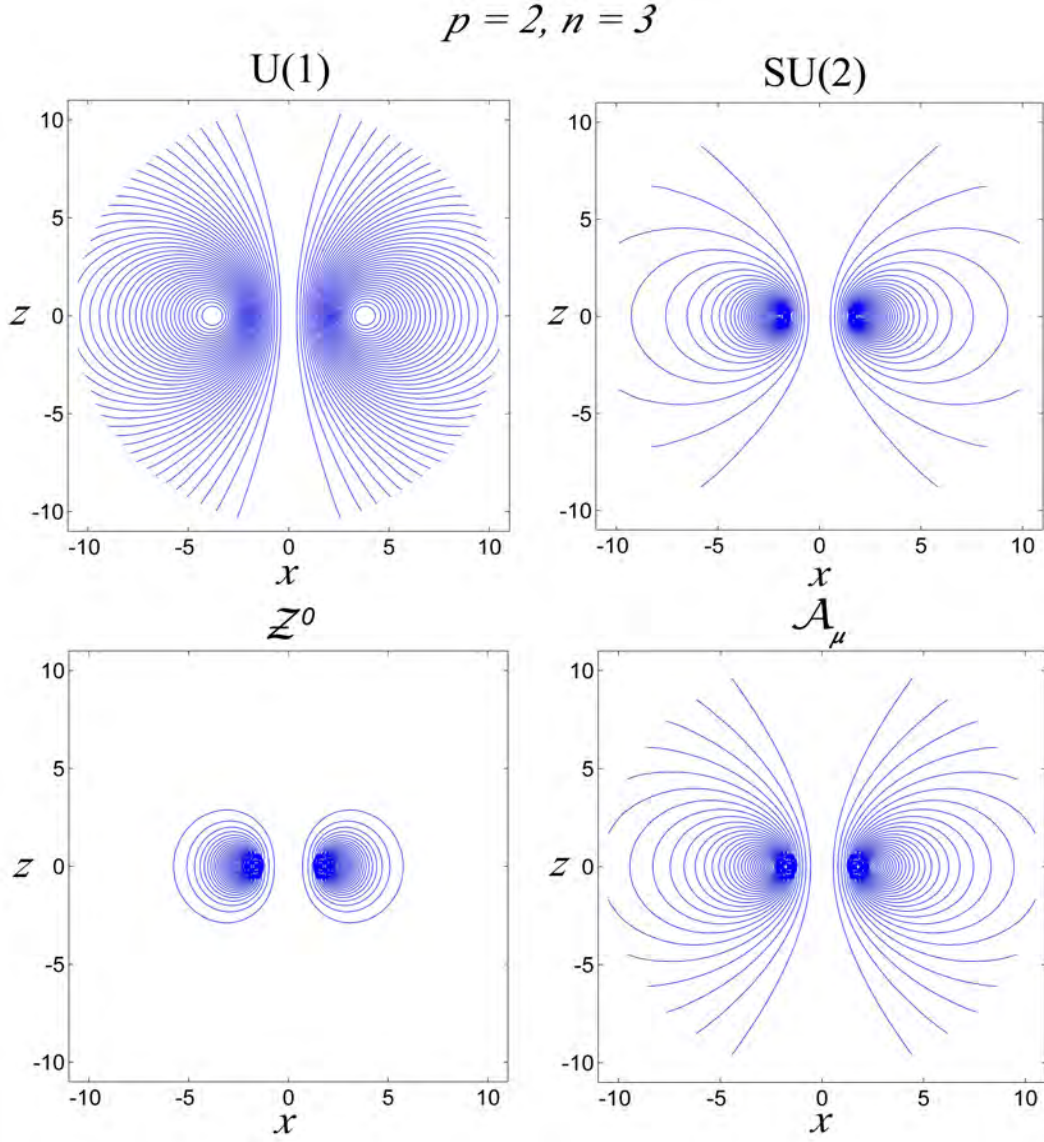


Figure 8: The contour line plot of the U(1), SU(2) 't Hooft, neutral \mathcal{Z}^0 , and electromagnetic field lines for the 1-MAP configuration along the x - z plane when $p = 2, n = 3$. Here $\mu = g\zeta = 1$ and $\theta_W = \frac{\pi}{4}$.

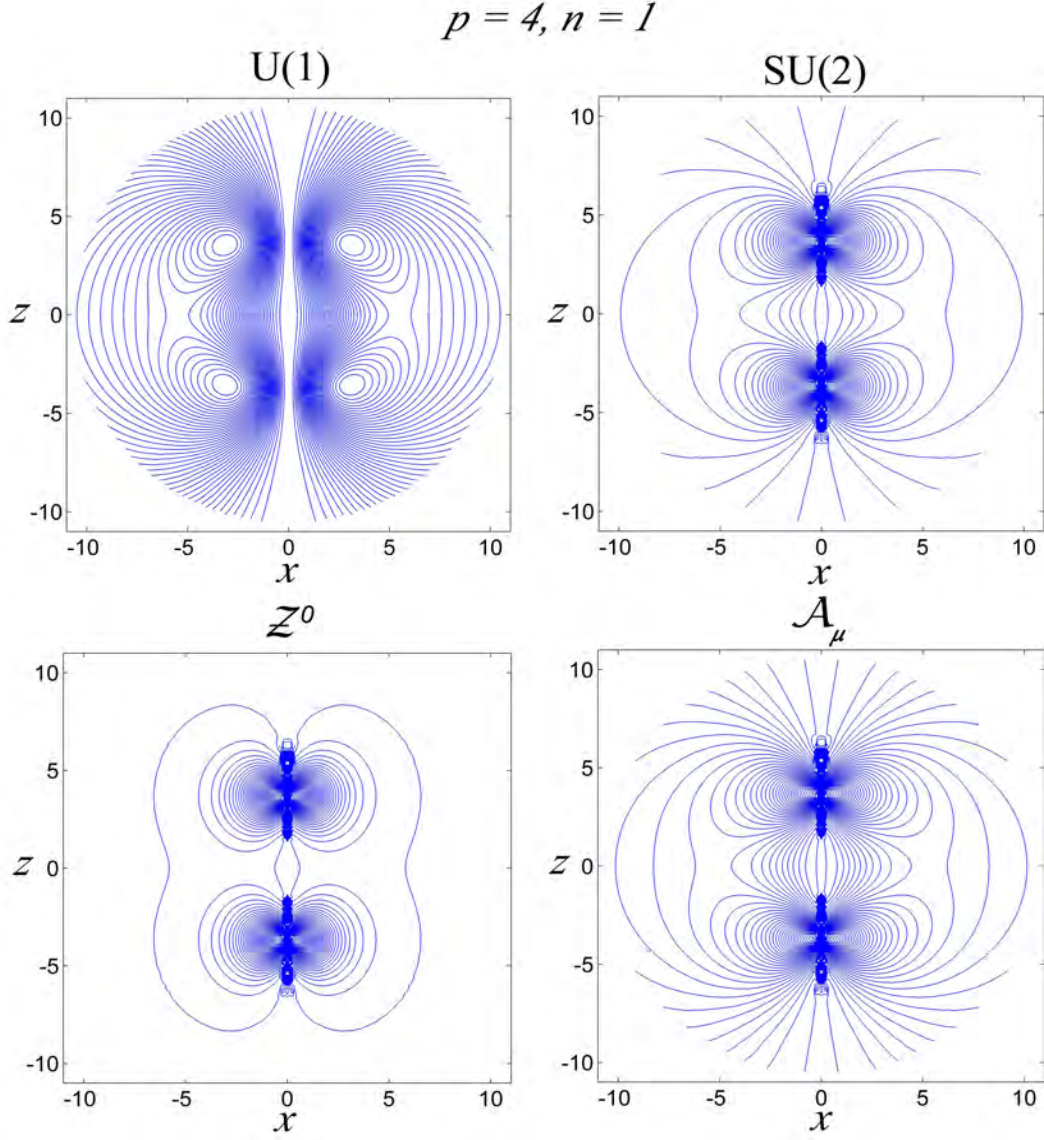


Figure 9: The contour line plot of the U(1), SU(2) 't Hooft, neutral \mathcal{Z}^0 , and electromagnetic field lines for the 2-MAP configuration along the x - z plane when $p = 4, n = 1$. Here $\mu = g\zeta = 1$ and $\theta_W = \frac{\pi}{4}$.

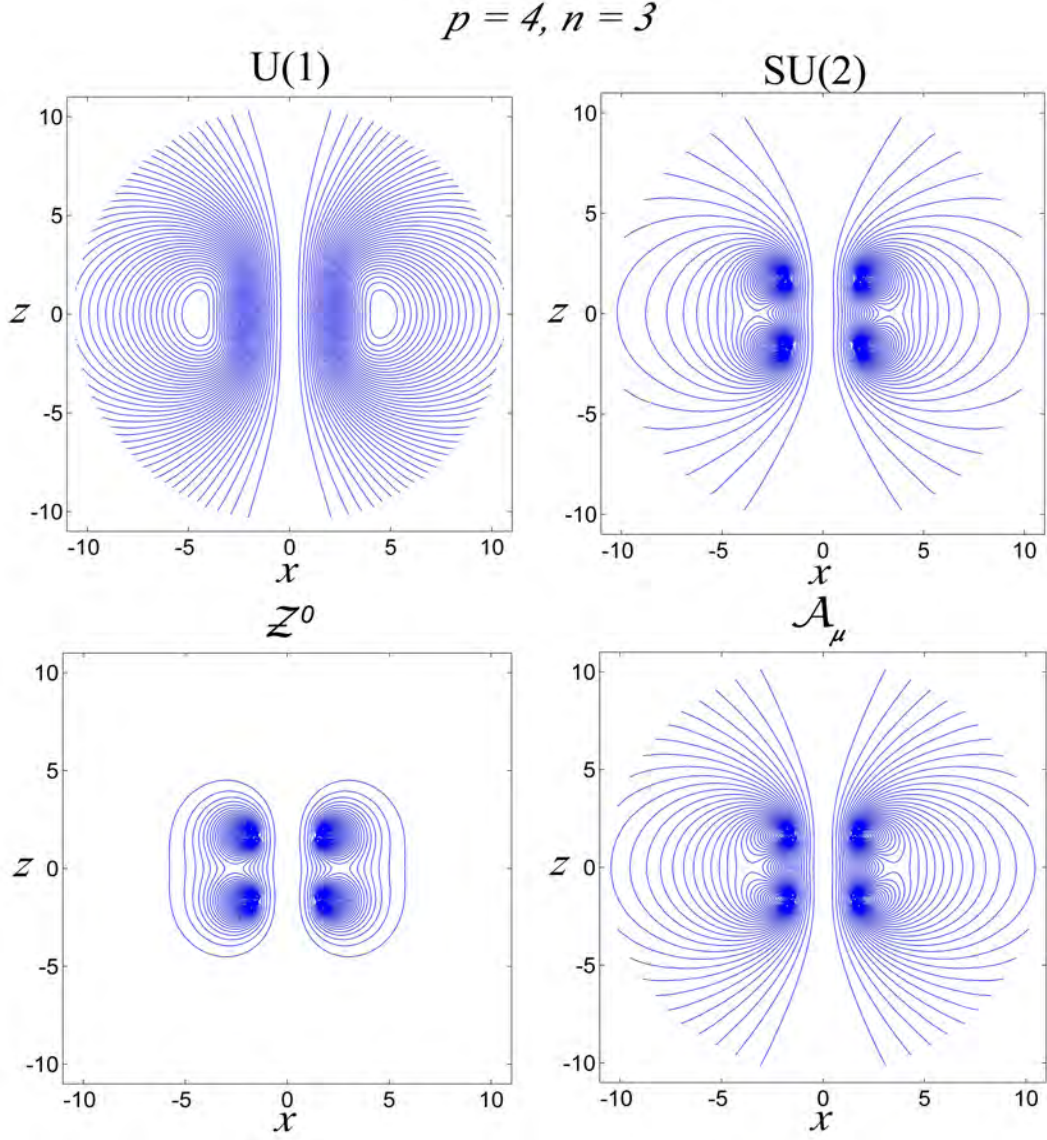


Figure 10: The contour line plot of the U(1), SU(2) 't Hooft, neutral \mathcal{Z}^0 , and electromagnetic field lines for the 2-MAP configuration along the x - z plane when $p = 4, n = 3$. Here $\mu = g\zeta = 1$ and $\theta_W = \frac{\pi}{4}$.